JCI The Journal of Clinical Investigation

Tricellulin deficiency affects tight junction architecture and cochlear hair cells

Gowri Nayak, … , Gregory I. Frolenkov, Saima Riazuddin

J Clin Invest. 2013;123(9):4036-4049. https://doi.org/10.1172/JCI69031.

Research Article

The two compositionally distinct extracellular cochlear fluids, endolymph and perilymph, are separated by tight junctions that outline the scala media and reticular lamina. Mutations in *TRIC* (also known as *MARVELD2*), which encodes a tricellular tight junction protein known as tricellulin, lead to nonsyndromic hearing loss (DFNB49). We generated a knockin mouse that carries a mutation orthologous to the *TRIC* coding mutation linked to DFNB49 hearing loss in humans. Tricellulin was absent from the tricellular junctions in the inner ear epithelia of the mutant animals, which developed rapidly progressing hearing loss accompanied by loss of mechanosensory cochlear hair cells, while the endocochlear potential and paracellular permeability of a biotin-based tracer in the stria vascularis were unaltered. Freeze-fracture electron microscopy revealed disruption of the strands of intramembrane particles connecting bicellular and tricellular junctions in the inner ear epithelia of tricellulin-deficient mice. These ultrastructural changes may selectively affect the paracellular permeability of ions or small molecules, resulting in a toxic microenvironment for cochlear hair cells. Consistent with this hypothesis, hair cell loss was rescued in tricellulin-deficient mice when generation of normal endolymph was inhibited by a concomitant deletion of the transcription factor, *Pou3f4*. Finally, comprehensive phenotypic screening showed a broader pathological phenotype in the mutant mice, which highlights the non-redundant roles played by tricellulin.

 Related Commentary, page 3712

Tricellulin deficiency affects tight junction architecture and cochlear hair cells

Gowri Nayak,[1] Sue I. Lee,[2] Rizwan Yousaf,[1] Stephanie E. Edelmann,[3] Claire Trincot,[1] Christina M. Van Itallie,[4] Ghanshyam P. Sinha,[3] Maria Rafeeq,[5] Sherri M. Jones,[6] Inna A. Belyantseva,[2] James M. Anderson,[4] Andrew Forge,[7] Gregory I. Frolenkov,[3] and Saima Riazuddin[1]

[1]Laboratory of Molecular Genetics, Division of Pediatric Otolaryngology / Head and Neck Surgery, Cincinnati Children's Hospital Research Foundation, and Department of Otolaryngology, College of Medicine, University of Cincinnati, Cincinnati, Ohio, USA. [2]Section on Human Genetics, Laboratory of Molecular Genetics, National Institute on Deafness and Other Communication Disorders, NIH, Rockville, Maryland, USA. [3]Department of Physiology, University of Kentucky, Lexington, Kentucky, USA. [4]National Heart, Lung, and Blood Institute, NIH, Bethesda, Maryland, USA. [5]National Center of Excellence in Molecular Biology, University of the Punjab, Lahore, Pakistan. [6]Department of Special Education and Communication Disorders, University of Nebraska, Omaha, Nebraska, USA. [7]Centre for Auditory Research, University College London, London, United Kingdom.

The two compositionally distinct extracellular cochlear fluids, endolymph and perilymph, are separated by tight junctions that outline the scala media and reticular lamina. Mutations in *TRIC* (also known as *MARVELD2*), which encodes a tricellular tight junction protein known as tricellulin, lead to nonsyndromic hearing loss (DFNB49). We generated a knockin mouse that carries a mutation orthologous to the *TRIC* coding mutation linked to DFNB49 hearing loss in humans. Tricellulin was absent from the tricellular junctions in the inner ear epithelia of the mutant animals, which developed rapidly progressing hearing loss accompanied by loss of mechanosensory cochlear hair cells, while the endocochlear potential and paracellular permeability of a biotin-based tracer in the stria vascularis were unaltered. Freeze-fracture electron microscopy revealed disruption of the strands of intramembrane particles connecting bicellular and tricellular junctions in the inner ear epithelia of tricellulin-deficient mice. These ultrastructural changes may selectively affect the paracellular permeability of ions or small molecules, resulting in a toxic microenvironment for cochlear hair cells. Consistent with this hypothesis, hair cell loss was rescued in tricellulin-deficient mice when generation of normal endolymph was inhibited by a concomitant deletion of the transcription factor, *Pou3f4*. Finally, comprehensive phenotypic screening showed a broader pathological phenotype in the mutant mice, which highlights the non-redundant roles played by tricellulin.

Introduction

Epithelial cells outline the lumen and surfaces of organs in the body and most commonly act as barriers between two different physiological environments. The barrier property of epithelial cells is due to structural specializations known as tight junctions between lateral membranes of adjacent cells. Tight junctions prevent the passage of solute and water molecules through the intercellular spaces between neighboring epithelial cells, a property known as barrier function, which varies with the requirements of the epithelial cells involved and the types of tight junction proteins expressed (1–3). While forming physical barriers within the plasma membrane, tight junctions also act as molecular fences and prevent the lateral diffusion of integral membrane proteins across the tight junctions (4, 5). Additionally, tight junctions have been shown to be involved in signal transduction pathways that regulate epithelial cell proliferation, differentiation, and morphogenesis (6). Tight junctions are dynamic structures that are continually being modified based on internal and external cues (7). Tight junctions between 2 adjacent cells are known as bicellular tight junctions, while tricellular tight junctions are observed at the site in which 3 epithelial cells meet. Freeze-fracture electron microscopy images reveal bicellular tight junctions as anastomosing strands of intramembranous particles, which seal the paracellular space in the plane of the epithelium (5). Tricellular tight junctions run perpendicular to the plane of epithelium and involve additional strands of intramembrane particles. At the point of contact of 3 cells, the topmost strands of the bicellular tight junctions turn in the basal direction, while additional vertically oriented tight junction strands form the "central sealing element" of the tricellular tight junction (8–11). At the center of the tricellular tight junction is a narrow tube that is involved in controlling paracellular flux of macromolecules (8–11).

Tight junctions between epithelial cells lining the scala media play an important role in compartmentalizing the endolymph and perilymph, the compositionally distinct inner ear fluids (12, 13). The endolymph, which is high in K^+ and low in Na^+, fills the scala media compartment of the cochlea and bathes the apical surfaces of hair cells. The endolymph in the cochlea is maintained at a high positive endocochlear potential (EP) of approximately 80 mV (14, 15). The perilymph, which is low in K^+ and high in Na^+, fills the scala tympani and vestibuli and bathes the basolateral surfaces of hair cells. Over recent decades, several of the proteins associated with tight junctions have been identified. While most are integral membrane proteins, some, like zonula occludens-1 (ZO-1), ZO-2, and ZO-3, are membrane-associated intracellular proteins, which connect the transmembrane tight junction proteins to cytoskeletal proteins, signaling molecules, and other membrane proteins (5, 16, 17). Among the integral membrane proteins are the claudins, occludin, tricellulin, marvelD3, junctional adhesion molecules,

Conflict of interest: The authors have declared that no conflict of interest exists.
Citation for this article: *J Clin Invest.* 2013;123(9):4036–4049. doi:10.1172/JCI69031.

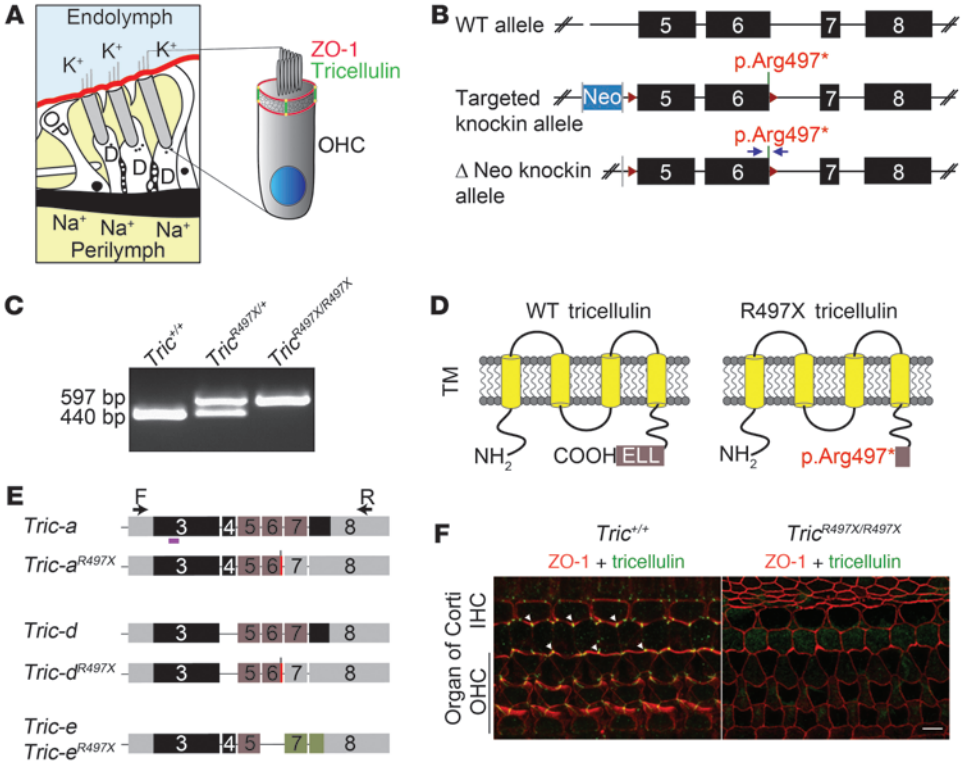

Figure 1

p.Arg497* mutation results in loss of tricellulin from the organ of Corti. (**A**) Schematic of organ of Corti cross-section, showing the tight junctions that separate endolymph (blue) from perilymph (yellow). At tricellular junctions, tricellulin (green) spans the entire depth of the cuticular plate and intersects ZO-1 (red) at apical and basal ends of these junctions. OP, outer pillar cell; D, Deiters' cell. (**B**) Scheme for generating the *Tric*$^{R497X/R497X}$ mice. Exons 5 and 6 were flanked by LoxP (red arrowheads) sites, and the neomycin selection cassette (Neo) that was flanked by FRT sites (gray bars) was removed by crossing *Tric*$^{R497X/R497X}$ mice with mice expressing Flp recombinase gene (59). The blue arrows represent the primers used to genotype the knockin mice. (**C**) PCR detection of wild-type allele (440 bp) and targeted allele (579 bp). (**D**) Schematic of the wild-type prematurely truncated tricellulin that is expected from the targeted allele. TM, transmembrane domain. (**E**) Schematics of transcripts (*a*, *d*, and *e*) that were amplified by RT-PCR from *Tric*$^{+/+}$ and *Tric*$^{R497X/R497X}$ inner ear cDNA and the location of the primers used for the reaction (arrows). Gray boxes indicate untranslated regions, and other colored boxes depict coding exons. *Tric-a* and *Tric-d* from *Tric*$^{R497X/R497X}$ inner ear cDNA had the knockin mutation (red bars). Brown exons encode the occludin-ELL domain. The magenta bar shows the location of the peptide used to generate the tricellulin antibody, PB705 (24). (**F**) Tricellulin (green) is absent from tricellular junctions in the organ of Corti of *Tric*$^{R497X/R497X}$ mice. Scale bar: 5 μm.

and the coxsackie and adenovirus-associated receptor (5). There are 24 claudins that have been identified so far, and these proteins form the backbone of tight junctions (5). Cis (intramembrane) and trans (intermembrane) interactions of claudin molecules are thought to give tight junctions the characteristic ultrastructure described above (5, 18, 19). Occludin, tricellulin, and marvelD3 belong to the family of MARVEL domain proteins and have been reported to have distinct, yet overlapping, functions in epithelial cell lines (5, 8, 20, 21). Physical interactions between tight junction proteins provide additional complexity to the tight junction structure and modify its permeability (5, 16, 18, 19, 22).

Tricellulin is found concentrated mostly at tricellular tight junctions, although weak labeling at bicellular tight junctions is seen depending on the type of epithelia being studied (8, 10, 23, 24). Occludin and lipolysis-stimulated lipoprotein receptor have been reported to affect the localization of tricellulin (25, 26). Although the actual role of tricellulin in barrier function has not been unequivocally demonstrated, studies on epithelial cell lines suggest that the overexpressed protein controls paracellular movement of macromolecules at tricellular tight junctions, whereas its presence at bicellular tight junctions modulates ion permeation (8, 9, 20, 27). However, when tricellulin was knocked down in epithelial cell lines EpH4 and Caco-2 using RNA interference, the cells exhibited significant delays in achieving transepithelial resistance (8, 20). In the mouse organ of Corti, tricellulin localizes specifically to the tricellular junctions, in which the fine "zipper-like" structures that make up these junctions span a region of approximately 3 to 5 μm, the entire depth of the reticular lamina (24).

Five different mutations in *TRIC*, encoding tricellulin, have been reported to cause autosomal recessive nonsyndromic deafness, DFNB49, in 14 families from Pakistan and Czech Roma populations (24, 28, 29). To determine the function of tricellulin in the inner ear and to elucidate the mechanism leading to hearing loss in the human families, we generated the corresponding knockin mouse model (p.Arg497*) for the only coding DFNB49 mutation (p.Arg500*). p.Arg497* mutation is predicted to result in loss of the C-terminal occludin-ELL domain, producing truncated protein. The current study demonstrates that the loss of full-length tricellulin disrupts the strands of intramembranous particles connecting bicellular and tricellular tight junctions in the inner ear epithelia of these mice and leads to the loss of mechanosensory hair cells in the organ of Corti.

Results

Tric$^{R497X/R497X}$ *mice do not express tricellulin at the tricellular tight junctions in the inner ear sensory epithelium.* Tricellulin (also known as MARVELD2) is seen at the tricellular junctions of all epithelial cells that outline the scala media in the cochlea (24). At these cellular junctions, tricellulin immunoreactivity can be seen along the depth of the tricellular junctions, intersecting the junctional "rings" formed by ZO-1 that is present at bicellular junctions (Figure 1A and ref. 24). In order to study the effect of the nonsense mutation in tricellulin underlying DFNB49, a knockin mouse model (*Tric*$^{R497X/R497X}$) was generated (Figure 1, B and C, and Sup-

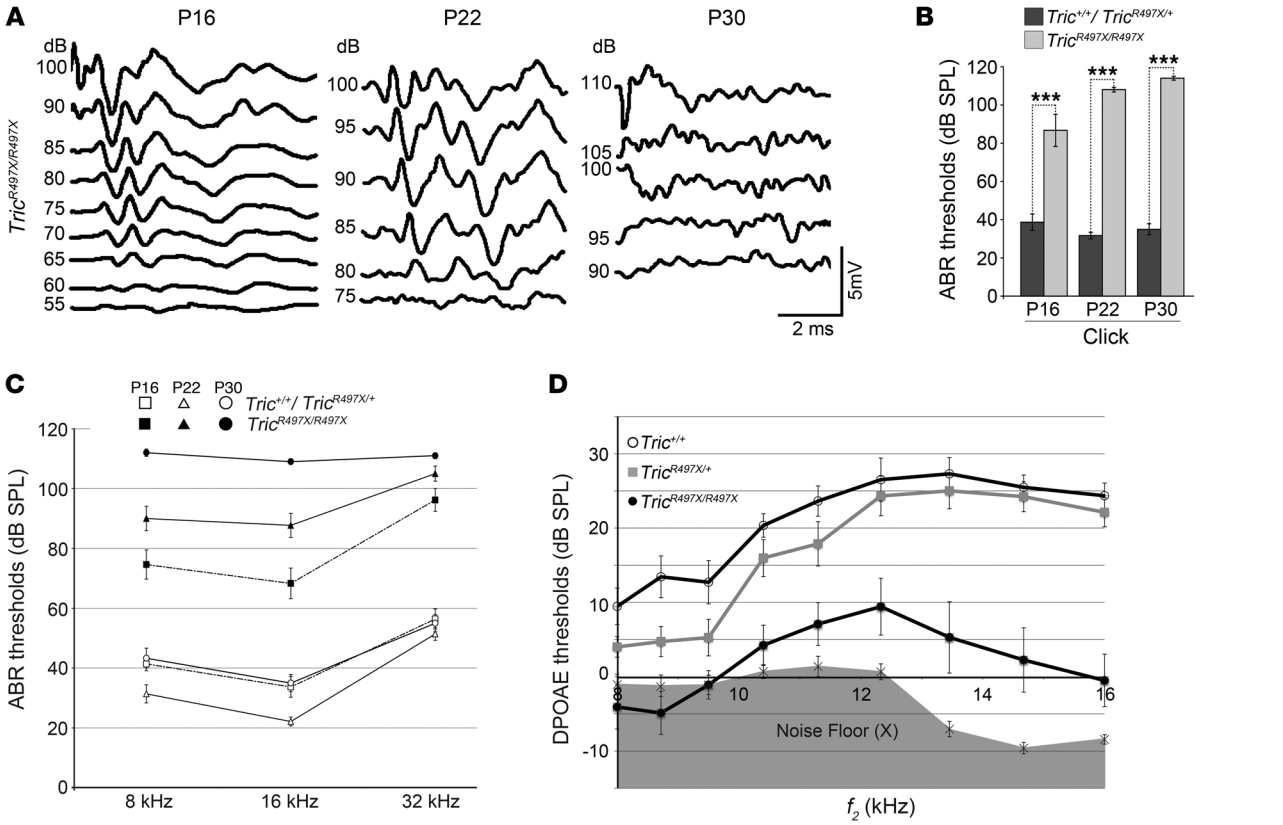

Figure 2

The *Tric*$^{R497X/R497X}$ mice are profoundly deaf by P30. (**A**) Representative ABR waveforms of *Tric*$^{R497X/R497X}$ mice in response to a click stimulus at the indicated ages. (**B**) Averaged ABR thresholds of *Tric*$^{R497X/R497X}$ mice and control littermates (*Tric*$^{R497X/+}$ and *Tric*$^{+/+}$) at P16, P22, and P30 in response to broadband click stimuli with SPL of 0 to 120 dB. The *Tric*$^{R497X/R497X}$ mice showed statistically significant (***$P < 0.0001$) elevated thresholds compared with control littermates (*Tric*$^{R497X/+}$ and *Tric*$^{+/+}$) at all 3 time points (P16, P22, and P30) tested (mean ± SEM; $n = 3$ for *Tric*$^{+/+}$ and *Tric*$^{R497X/+}$ mice, $n = 5$ for *Tric*$^{R497X/R497X}$ mice). (**C**) Averaged ABR thresholds of *Tric*$^{R497X/R497X}$ mice (black symbols) and control littermates (*Tric*$^{R497X/+}$ and *Tric*$^{+/+}$, white symbols) at P16, P22, and P30 in response to tone-bursts of 8 kHz, 16 kHz, and 32 kHz. The *Tric*$^{R497X/R497X}$ mice showed statistically significant ($P < 0.0001$) elevated thresholds compared with control littermates (*Tric*$^{R497X/+}$ and *Tric*$^{+/+}$) for all frequencies at all time points (P16, P22, and P30) tested (mean ± SEM; $n = 10$ for *Tric*$^{+/+}$, *Tric*$^{R497X/+}$, and *Tric*$^{R497X/R497X}$ mice). (**D**) DPOAEs of P16 *Tric*$^{+/+}$ (white circles), *Tric*$^{R497X/+}$ (gray squares), and *Tric*$^{R497X/R497X}$ (black circles) mice represented as a function of f_2 stimulus frequencies, ranging from 8 kHz to 16 kHz. *Tric*$^{R497X/R497X}$ mice showed attenuated responses, but the values were mostly above the noise floor (X), indicating that the residual OHCs seen at this age are functional (mean ± SEM; $n = 8$ for *Tric*$^{+/+}$ and *Tric*$^{R497X/+}$ mice, $n = 13$ for *Tric*$^{R497X/R497X}$ mice).

plemental Table 1; supplemental material available online with this article; doi:10.1172/JCI69031DS1).

Like the other MARVEL domain proteins, tricellulin is a multipass transmembrane protein, with cytosolic N- and C-termini (Figure 1D) (8, 24). The C terminus contains an occludin-ELL domain, and the p.Arg497* knockin mutation is predicted to prematurely terminate the protein, resulting in loss of the occludin-ELL domain (Figure 1D). RT-PCR analysis of inner ear cDNA from wild-type and *Tric*$^{R497X/R497X}$ mice revealed various transcripts of *Tric*, some of which are predicted to be affected by the knockin allele (Figure 1E). *Tric-a* isoform has been reported before (24) and was also found in our RT-PCR screen in both *Tric*$^{+/+}$ and *Tric*$^{R497X/R497X}$ samples, where the latter had the knockin mutation. *Tric-d* and *Tric-e* have not been reported previously. *Tric-d* lacks cassette exon 4, while exon 6 is alternatively spliced in *Tric-e*, resulting in an alternate reading frame. Real-time quantitative PCR analysis (Supplemental Table 1) revealed statistically significant upregulation of most of these isoforms in *Tric*$^{R497X/R497X}$ mutant mice at P10 (Supplemental Figure 1A). These results suggest that *Tric* mRNA with the premature stop codon does not degrade through a nonsense-mediated mRNA decay pathway (30).

Western blotting with tricellulin polyclonal antibody showed detectable levels of tricellulin in the inner ear protein lysates of P10 *Tric*$^{+/+}$ and *Tric*$^{R497X/+}$ mice but not in the inner ear protein lysates of P10 *Tric*$^{R497X/R497X}$ animals (Supplemental Figure 1B). Immunolabeling using the previously validated antiserum PB705 (24) revealed that tricellulin immunoreactivity was lost from the tricellular tight junctions in the sensory (Figure 1F and Supplemental Figure 2) as well as all nonsensory (data not shown) epithelia of the cochleae and vestibular organs of *Tric*$^{R497X/R497X}$ mice. The weak intracellular labeling in the *Tric*$^{+/+}$ and *Tric*$^{R497X/R497X}$ organ of Corti may be nonspecific or correspond to truncated protein or the protein product of splice isoform *e*, which should be unaffected by the nonsense mutation (Figure 1F). Thus, the premature stop codon may result in a protein product that lacks a targeting sequence required for localization or retaining mutant protein at the tricel-

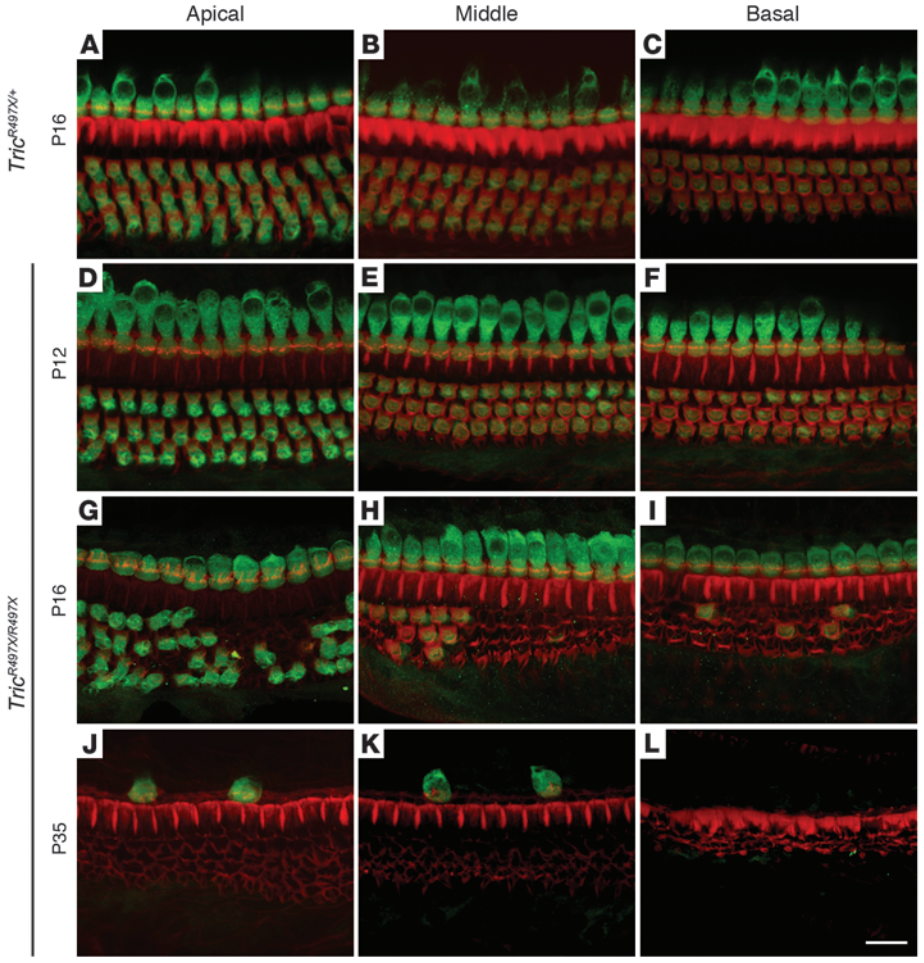

Figure 3
OHCs in the *Tric*$^{R497X/R497X}$ mice undergo rapid degeneration in the third and fourth weeks of life. Maximum intensity projections of confocal Z-stacks of cochlear whole mounts labeled with myoVIIa antibody (green) and counterstained with phalloidin labeling of cytoskeletal filamentous actin (red) are shown. (**A**–**C**) Representative images from the apical, middle, and basal turns of the organ of Corti of a *Tric*$^{R497X/+}$ (control) mouse at P16. (**D**–**L**) Images of the organ of Corti from the 3 turns of the cochlea of *Tric*$^{R497X/R497X}$ mice at (**D**–**F**) P12, (**G**–**I**) P16, and (**J**–**L**) P35. While the hair cells appear to have normal development and morphology at P12 in the knockin mice, severe OHC degeneration can be seen by P16. The OHC loss progresses rapidly, followed by IHC loss. By P35, only few IHCs remain in the apical and middle turns of the cochlea. Scale bar: 10 μm.

lular junctions. To test this hypothesis, Madin-Darby canine kidney (MDCK) cells were transfected with the plasmid constructs encoding the full-length wild-type and p.Arg500* mutant tricellulin, both fused to GFP at the N terminus (Supplemental Figure 3A). In cells with higher expression levels of TRIC^{WT}, the protein was enriched at tricellular tight junctions (Supplemental Figure 3A). In contrast, TRIC^{R500X} only localized to the basolateral membrane and sometimes to the bicellular tight junctions, in which occasionally the protein was found concentrated in discrete puncti but not at the tricellular junctions (Supplemental Figure 3B). Thus, our in vivo (knockin mouse) and ex vivo (transiently transfected MDCK cell) studies suggest that tricellulin with a truncated carboxy terminus is unable to localize to tricellular tight junctions.

Tric$^{R497X/R497X}$ *mice have rapidly progressing hearing loss and are profoundly deaf by P30*. In order to determine the cochlear function of *Tric*$^{R497X/R497X}$ mice, their auditory brainstem responses (ABRs) were measured using broadband click and tone-burst sounds at 3 different time points, P16, P22, and P30 (Figure 2, A–C). Compared with heterozygous mice, the *Tric*$^{R497X/R497X}$ mice had elevated ABR thresholds ($P < 0.0001$) as early as P16 at all the frequencies tested (Figure 2, B and C). The hearing phenotype was found to worsen over the next few days, and the knockin mice were profoundly deaf across all frequencies by P30 (Figure 2, B and C). Thus, the hearing loss seen in these animals is early onset and rapidly progressive, involving the entire cochlea within the third week of life.

To explore the function of the cochlear outer hair cells (OHCs) in *Tric*$^{+/+}$, *Tric*$^{R497X/+}$, and *Tric*$^{R497X/R497X}$ mice, we recorded distortion product otoacoustic emissions (DPOAEs), which are generated by OHCs in response to auditory stimuli at different frequencies (Figure 2D). At P16–P17, the *Tric*$^{+/+}$ and *Tric*$^{R497X/+}$ mice generated similar DPOAEs. However, the *Tric*$^{R497X/R497X}$ mice had attenuated DPOAEs of varying degrees compared with those of the controls, although the amplitudes of the emissions were often discernible from the noise floor (Figure 2D). Taken together with ABRs, these results suggest that hearing loss in *Tric*$^{R497X/R497X}$ mice is likely to result from peripheral (cochlear) deficiencies.

The p.Arg497 mutation in tricellulin leads to progressive hair cell degeneration by the third week of life*. Next, we examined the morphology of the cochlear epithelium at various postnatal developmental stages to determine the underlying cause of hearing loss observed in the *Tric*$^{R497X/R497X}$ mice. Confocal microscopy revealed no differences in morphology of OHCs and inner hair cells (IHCs) in P12 *Tric*$^{R497X/R497X}$ and *Tric*$^{R497X/+}$ control mice (Figure 3, A–F, and Supplemental Figure 4, A–F). By P16, however, varying degrees of OHC degeneration were observed along the length of the cochlea, although the IHCs appeared largely intact, as seen by phalloidin labeling (Figure 3, G–I, and Supplemental Figure 4, G–I). By P35, there were no OHCs visible and very few IHCs that were confined to the apical and middle turns of the cochlea (Figure 3, J–L, and Supplemental Figure 4, J–L). Furthermore, *Tric*$^{R497X/R497X}$ OHCs demonstrated proper acquisition of prestin (Supplemental Figure 4), which indicates likely normal electromotile function of OHCs in these mice during early postnatal development. The degeneration pattern observed by immunofluorescence was confirmed by scanning electron microscopy examination of the morphology of the cochlear epithelium from *Tric*$^{R497X/+}$ and *Tric*$^{R497X/R497X}$ mice (Supplemental Figure 5).

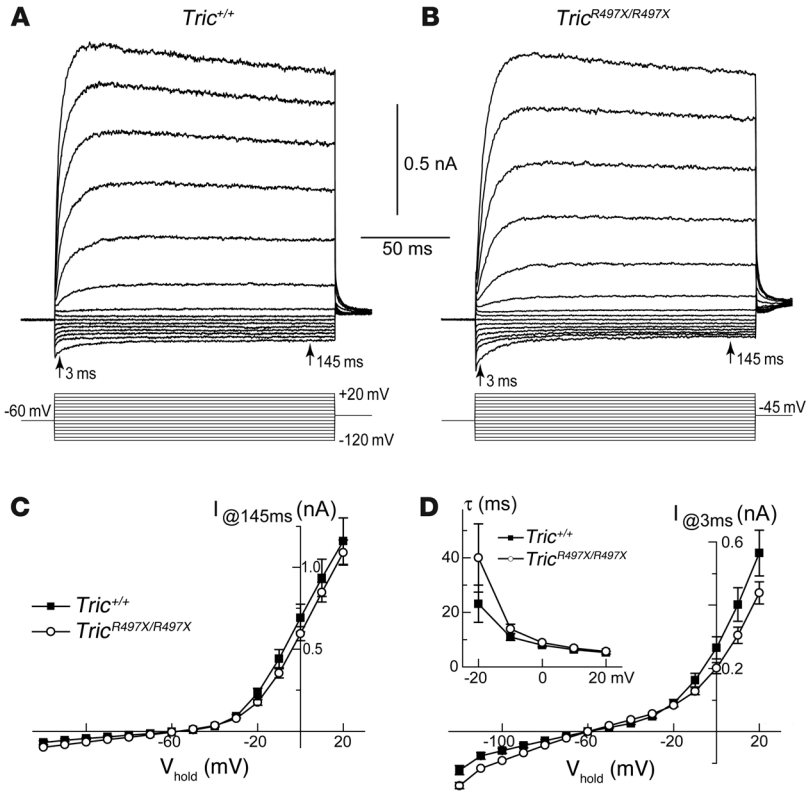

Figure 4
The p.Arg497* mutation does not affect the maturation of voltage-gated ion conductances in OHCs. (**A**) Whole-cell patch-clamp recordings of the outward and inward ionic conductances in OHCs of cochlear explants of *Tric*$^{+/+}$ mice. The membrane currents (top traces) were evoked by depolarizing and hyperpolarizing voltage steps (bottom traces) of various step potentials from –120 mV to +20 mV. OHCs were maintained at a holding potential of –60 mV between acquisitions. (**B**) Whole-cell currents in OHCs of the *Tric*$^{R497X/R497X}$ mice were comparable to those observed in OHCs of wild-type littermates. (**C**) The steady-state currents measured at 145 ms after onset of the voltage step were identical in OHCs of *Tric*$^{R497X/R497X}$ (white circles) and *Tric*$^{+/+}$ (black circles) mice. (**D**) Statistically nonsignificant differences in the speed of activation of voltage-gated conductances. The current response measured at 3 ms after beginning of the voltage step is shown. The differences in responses (mean ± SEM) of *Tric*$^{R497X/R497X}$ (white circles, $n = 21$) and *Tric*$^{+/+}$ (black circles, $n = 15$) OHCs were largely nonsignificant except at 1 point at –120 mV ($P < 0.05$). The inset shows the time constant (τ) of current activation. The same recordings contributed to **C** and **D**. The age of the cultured organ of Corti was P3 plus 3–5 days in vitro.

Scanning electron microscopy images reveal that the hair bundles and the apical surface of the reticular lamina of cochleae from *Tric*$^{R497X/R497X}$ mice appeared normal at P12 (Supplemental Figure 5). However, by P16, more OHCs were partially or completely degenerated, while IHCs were still present throughout the cochlea. By P30, nearly all hair cells were lost along the entire cochlear epithelium and the 3 rows of OHCs were replaced by supporting cells, while occasional IHCs with long fused stereocilia were still seen. The hair cell degeneration was followed by progressive degeneration of the spiral ganglion after P50 in *Tric*$^{R497X/R497X}$ mice (Supplemental Figure 6).

Voltage-gated ion conductances in OHCs of early postnatal Tric$^{R497X/R497X}$ *mice are normal*. Both immunofluorescence and scanning electron microscopy data revealed no structural abnormalities in OHCs of *Tric*$^{R497X/R497X}$ mice at P12 (Figure 3 and Supplemental Figures 4 and 5). In search for potential functional deficiencies that might precede structural changes, we used conventional whole-cell patch-clamp technique to record voltage-activated conductances in OHCs in the cultured organ of Corti explants of wild-type and *Tric*$^{R497X/R497X}$ mice at the equivalent age (dissection age plus time in vitro) of P6–P8 (Figure 4). Similar to previous reports (31), the outward and inward potassium currents could be already evoked in wild-type young postnatal OHCs at these ages (Figure 4A). Both outward and inward potassium currents were also recorded in OHCs of *Tric*$^{R497X/R497X}$ mice, and they were very similar to the wild-type currents (Figure 4B). The steady-state amplitude of the currents did not differ in wild-type and *Tric*$^{R497X/R497X}$ mice (Figure 4C). The activation of voltage-gated conductances was a bit slower, and inward conductance was slightly more prominent in *Tric*$^{R497X/R497X}$ OHCs, but all these differences were statistically nonsignificant (Figure 4D). We conclude that tricellulin deficiency does not affect the initial postnatal maturation of ion currents in young postnatal OHCs.

Ultrastructure of tricellular tight junctions is affected in the inner ear of Tric$^{R497X/R497X}$ *mice*. Loss of tricellulin from the tricellular tight junctions of the knockin mice may lead to structural changes in these cellular junctions (8). In order to determine the ultrastructure of tricellular tight junctions in the various epithelia of the inner ear of the knockin mice, freeze-fracture replica electron microscopy was performed (Figure 5 and Supplemental Figures 7 and 8). The ultrastructure of the tricellular tight junctions in the inner ear epithelia of control, *Tric*$^{+/+}$, and *Tric*$^{R497X/+}$ mice and the changes seen in the *Tric*$^{R497X/R497X}$ animals are depicted as schematics (Figure 5, A and B). The tricellular tight junctions in the organ of Corti of control samples (Figure 5C, arrows) showed the characteristic "fishbone-like" appearance, where intramembranous strands emerge from either side of a central ridge (Figure 5C, arrowheads). This "fishbone-like" feature is formed by the bicellular tight junction strands that turn to meet the central ridge of the tricellular junction roughly at right angles. Unlike the morphology seen in the *Tric*$^{+/+}$ and *Tric*$^{R497X/+}$ animals, the tricellular tight junction–like structures in the organ of Corti of *Tric*$^{R497X/R497X}$ mice appeared discontinuous and were formed by a series of particles that were arranged in an orderly but disconnected fashion (Figure 5D, arrows). Also, the "fishbone-like" appearance was absent, as the bicellular tight junction strands did not meet the central ridge of the tricellular junction in the *Tric*$^{R497X/R497X}$ mice (Figure 5D, arrowheads). Instead, in the *Tri*$^{cR497X/R497X}$ mice, the topmost elements of the bicellular junctions turned downward, running parallel to the central ridge of the tricellular junction, and joined the strands of adjacent bicellular junctions (Figure 5D, arrowheads).

A similar phenotype is seen at tricellular contacts in the utricular macula (vestibular organ) of *Tric*$^{R497X/R497X}$ mice (Figure 5, E–G). In *Tric*$^{R497X/+}$ mice, the central ridge of the tricellular junction was

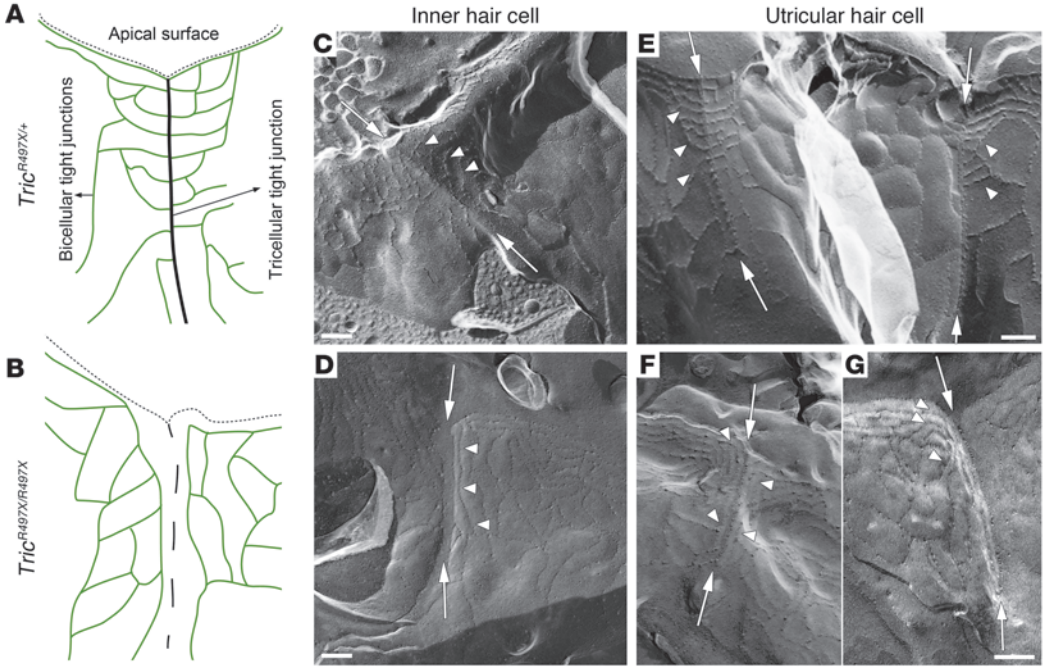

Figure 5
Tricellulin is required for the normal development of the tricellular junction structure. (**A** and **B**) Schematic representations of the ultrastructure of tight junctions in the inner ear epithelia of *Tric*$^{R497X/+}$ and *Tric*$^{R497X/R497X}$ mice. The thin dashed lines indicate the vertices of the apical surface. (**A**) In the controls, the bicellular tight junction strands (green) are associated with the tricellular tight junction (black line). (**B**) In the *Tric*$^{R497X/R497X}$ mice, the tricellular tight junction is not complete (dashed line). Also, the topmost bicellular tight junction strands turn downward and run parallel to the tricellular tight junction. (**C**–**G**) Electron microscopy images of freeze-fracture replica of tricellular tight junctions in the (**C** and **D**) organ of Corti and (**E**–**G**) utricular macula of (**C** and **E**) *Tric*$^{R497X/+}$ and (**D**, **F**, and **G**) *Tric*$^{R497X/R497X}$ mice. (**C** and **E**) In the *Tric*$^{R497X/+}$ animals, tricellular tight junctions appear as a "fishbone" (arrows), where the elements of the bicellular junctions meet the tricellular tight junction (arrowheads). (**D**, **F**, and **G**) In the *Tric*$^{R497X/R497X}$ animals, the central element of the tricellular junction is irregular and appears to be formed of a chain of disconnected particles (arrows). The bicellular tight junction strands do not meet the tricellular junction (arrowheads); instead, they appear to turn around and join the neighboring bicellular junction strands. Scale bar: 200 nm (**C**–**E**; **F** and **G**).

quite pronounced, with double rows of closely packed particles (Figure 5E, arrows), where the elements of the bicellular junctions merged with it (Figure 5E, arrowheads). In *Tric*$^{R497X/R497X}$ mice, there was some structure at tricellular contacts, but it was only a single line, and the particles were not as closely packed (Figure 5, F and G, arrows). Similar to the junctions in the organ of Corti of the knockin animals, the elements of the bicellular tight junction did not meet the structure at the tricellular junctions of the vestibular epithelium but rather turned to run parallel with the line of the junction between the 3 cells (Figure 5, F and G, arrowheads). It appeared that there was no continuity between the elements of the bicellular tight junctions and the central ridge of the tricellular junction.

The *Tric*$^{R497X/R497X}$ mutants also had alterations in the ultrastructure of the tricellular tight junctions in the marginal cells of the stria vascularis, similar to those seen in the organ of Corti and the vestibular epithelia of these animals (Supplemental Figure 8). These results show that tricellulin is indispensable for the normal formation of tricellular tight junctions in the various epithelia of the inner ear. Presence of discontinuous particles along the length of the tricellular tight junction in *Tric*$^{R497X/R497X}$ mutant mice suggests that tricellular tight junctions in the inner ear are complex and are composed of multiple proteins.

Changes in the ultrastructure of the tricellular tight junctions seen in the absence of tricellulin might also be due to defects in the cytoskeletal architecture or organization of other tight junction proteins. However, RT-PCR (data not shown) and immunofluorescence analyses revealed that there were no observable changes in the expression or localization of various tight junction and cytoskeletal proteins in the organ of Corti of *Tric*$^{R497X/R497X}$ mice at P2–P10 (Supplemental Figure 9). Moreover, the early postnatal development of the cochlear hair cells appeared to be unaffected in the *Tric*$^{R497X/R497X}$ mice (Figure 3, D–F, and Figure 4), which further supports the normal development of the hair cell cytoskeleton except tricellular tight junctions.

The barrier properties and function of the stria vascularis are unaffected in the Tric$^{R497X/R497X}$ *mice*. We observed thinning of the stria vascularis in 3-month-old tricellulin mutant mice compared with that in the heterozygous animals (Figure 6, A and B). Tight junctions of both basal and marginal cells of the stria vascularis are an integral part of the machinery that generates the EP. A deficit in the tricellular tight junctions between the marginal cells seen in tricellulin mutant mice (Supplemental Figure 8) may result in altered barrier properties of the stria vascularis and the EP. To investigate the paracellular permeability properties of the stria vascularis, tracer-permeability assays were performed using *Tric*$^{+/+}$ and *Tric*$^{R497X/R497X}$ mice at different ages (P30, P240, and P300). The biotin-based tracer was not found in the intrastrial space of *Tric*$^{+/+}$ and *Tric*$^{R497X/R497X}$ mice at any of the ages examined (Figure 6, C–J), suggesting that there are no barrier

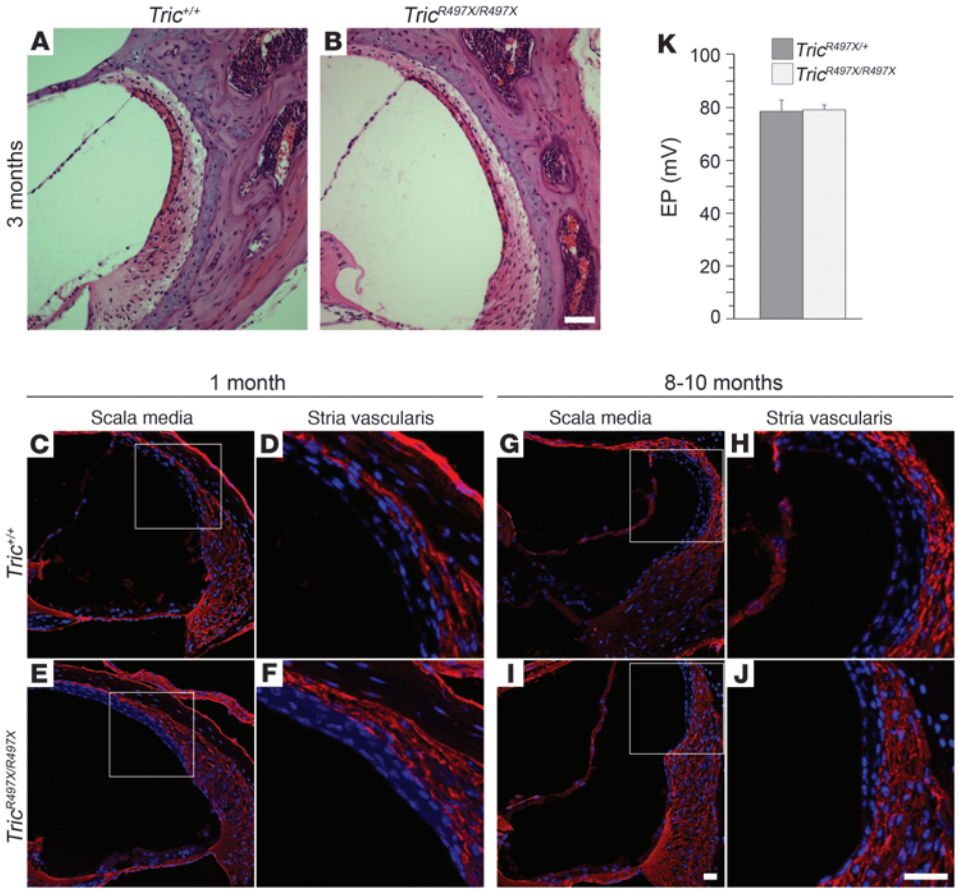

Figure 6
Stria vascularis function and barrier properties are normal in the *Tric*$^{R497X/R497X}$ mice. Hematoxylin and eosin labeling of paraffin-embedded inner ear sections showing (**A**) normal stria vascularis in 3-month-old *Tric*$^{+/+}$ mice and (**B**) the thinning of this tissue seen in the *Tric*$^{R497X/R497X}$ littermates. (**C**–**J**) Frozen sections made from (**C**, **D**, **G**, and **H**) *Tric*$^{+/+}$ and (**E**, **F**, **I**, and **J**) *Tric*$^{R497X/R497X}$ mice, respectively, after tracer injections into the oval and round windows of these animals at (**C**–**F**) 1 month and (**G**–**J**) 8 to 10 months of age. The biotin-based tracer molecule (in red) does not permeate through the basal cell layer of the stria vascularis in either the (**D** and **H**) *Tric*$^{+/+}$ or (**F** and **J**) *Tric*$^{R497X/R497X}$ mice. The nuclei of the intermediate and marginal cells are labeled with DAPI (blue). (**K**) EP in *Tric*$^{R497X/+}$ (dark gray bar) and *Tric*$^{R497X/R497X}$ (light gray bar) mice (mean ± SEM; n = 5 for *Tric*$^{R497X/+}$, n = 6 for *Tric*$^{R497X/R497X}$; age of the animals: P25–P36). Scale bar: 50 μm (**A** and **B**); 20 μm (**C**–**J**).

defects at the basal cell layer of the stria vascularis in the mutant mice. As an indicator of stria vascularis function, we measured the EP of adult (P25–P36) *Tric*$^{R497X/+}$ and *Tric*$^{R497X/R497X}$ mice (Figure 6K). Despite ultrastructural changes of tight junctions, as observed by freeze-fracture microscopy, EP was normal in *Tric*$^{R497X/R497X}$ mice (Figure 6K). Therefore, the changes in paracellular permeability in tricellulin-deficient epithelia must be relatively subtle. However, even subtle changes in permeability for important signaling molecules like ATP may result in abnormal activation of OHCs, leading to their death.

Vestibular function is intact in the Tric$^{R497X/R497X}$ *mice*. Immunolocalization studies in vestibular epithelia revealed that tricellulin is also expressed in these organs (24). Similar ultrastructural abnormalities were seen in the tricellular tight junctions in the vestibular and auditory sensory epithelia of the *Tric*$^{R497X/R497X}$ mice (Figure 5). Nevertheless, we did not observe any hair cell death in the vestibular organs of the *Tric*$^{R497X/R497X}$ mice (Supplemental Figure 10), and these animals did not display any obvious vestibular defects based on the lack of head bobbing and circling. Moreover, vestibular-evoked potentials recorded from *Tric*$^{R497X/+}$ and *Tric*$^{R497X/R497X}$ mice at P30 and P150 revealed no abnormality (Supplemental Figure 11). On average, the P1 latencies (Supplemental Figure 11C) and P1-N1 amplitudes (Supplemental Figure 11D) for *Tric*$^{R497X/R497X}$ mice were not significantly different from those of heterozygous littermates at both time points. Vestibular-evoked potential thresholds were also similar between P30 *Tric*$^{R497X/+}$ mice (–8.5 ± 1.7 dB relative to 1.0 g/ms) and *Tric*$^{R497X/R497X}$ mice (–9.5 ± 1.7 dB) and at P150 (–11.5 ± 1.7 dB for both genotypes). This suggests that tricellulin is dispensable in the vestibular organs, despite the ultrastructural changes that were observed in the tricellular tight junctions in these sensory epithelia. Previous studies have also shown that the cochlea is more susceptible to defects than the vestibular epithelia due to mutations in members of the claudin family of tight junction proteins (32–35). This probably reflects functional compensation in the latter epithelia by other tight junction proteins.

The hair cell degeneration phenotype due to the p.Arg497 mutation is rescued in Tric*$^{R497X/R497X}$*: Pou3f4*^{delJ} *double mutants*. Loss of cochlear hair cells in *Tric*$^{R497X/R497X}$ mice may be due to disrupted cell signaling or altered microenvironment around these cells. Mice deficient in the transcription factor POU3F4 (*Pou3f4*^{delJ}) have reduced EP and early-onset profound hearing loss but do not have any defects in the organ of Corti (36). *Pou3f4*^{delJ} mice exhibit defects in both the otic fibrocytes, cells thought to be responsible for K^+ recycling, and expression of KIR 4.1 channels that are necessary for the generation of the EP and normal ionic composition of the endolymph (37). Therefore, we generated *Tric* and *Pou3f4* double-mutant animals to test whether dramatic changes in the endolymph composition would rescue the hair cell degeneration in *Tric*$^{R497X/R497X}$ mice. *Pou3f4* is located on the X-chromosome, and double-mutant mice that were homozygous for the p.Arg497X* mutation and were hemizygous (male) or homozygous (female) for the *Pou3F4* deletion (*Tric*$^{R497X/R497X}$*: Pou3f4*^{delJ}) were analyzed. At P16, compared with control littermates (Figure 7, A–D), *Tric*$^{R497X/R497X}$ mice showed severe OHC degeneration (Figure 7, E–H). In *Tric*$^{R497X/R497X}$*: Pou3f4*^{delJ} double-mutant mice, myosin VIIa labeling showed no degeneration of OHCs in the cochleae of these mice at P16 (Figure 7, I–L). These

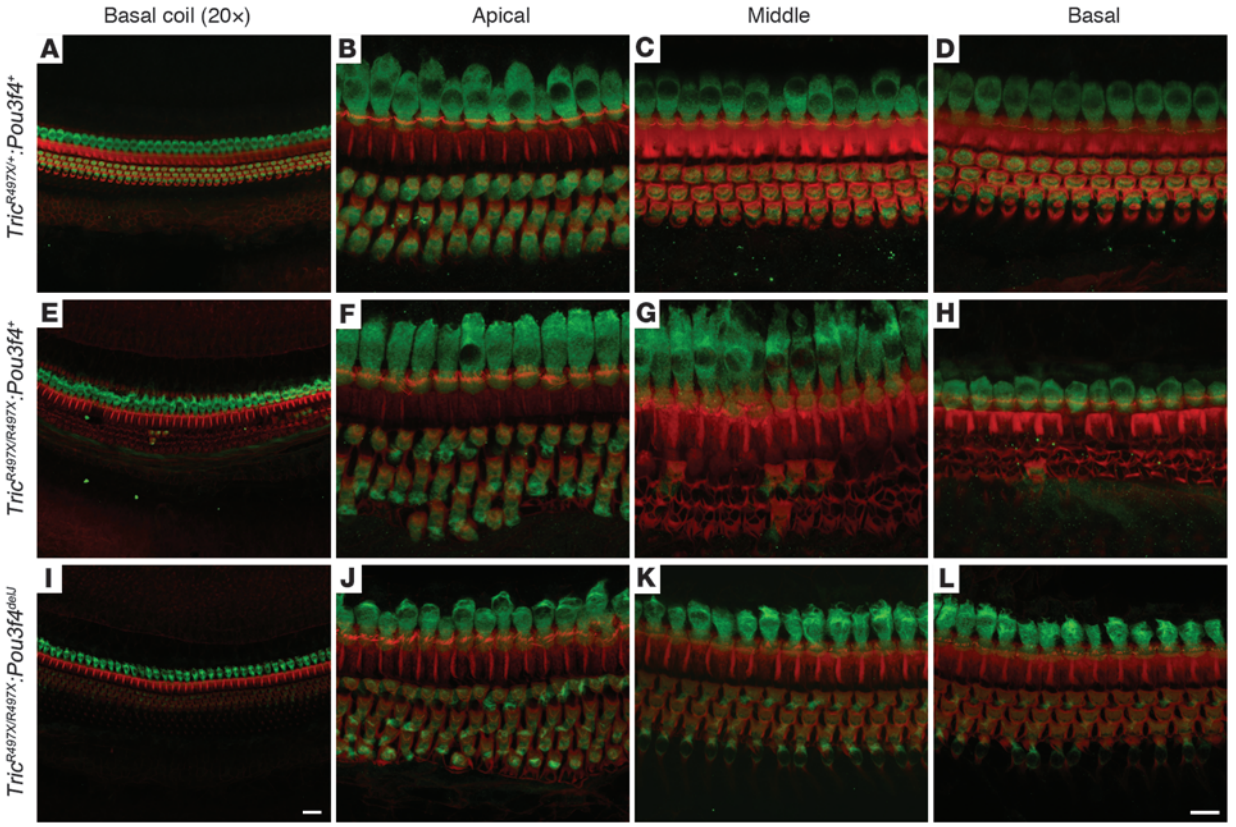

Figure 7
The OHC degeneration is rescued in *Tric*$^{R497X/R497X}$*: Pou3f4*^{delJ} double mutants. Maximum intensity projections of (**A**, **E**, and **I**) low-magnification and (**B**–**D**, **F**–**H**, and **J**–**L**) high-magnification confocal images of cochlear sensory epithelia labeled with an antibody against a hair cell marker, myosin VIIa (green), and counterstained with rhodamine phalloidin (red). (**A**–**D**) Images of the organ of Corti from the 3 turns of the cochleae of P16 *Tric*$^{R497X/+}$*: Pou3f4*$^{+}$ mice. (**E**–**H**) Images of the organ of Corti in the 3 turns of the cochleae of P16 *Tric*$^{R497X/R497X}$*: Pou3f4*$^{+}$ mice, which show the extent of OHC degeneration in these mice. (**I**–**L**) Images of the organ of Corti in the 3 turns of the cochleae of P16 *Tric*$^{R497X/R497X}$*: Pou3f4*^{delJ} double-mutant mice. The OHC degeneration is rescued in the double mutants. Scale bar: 20 μm (**A**, **E**, and **I**); 10 μm (**B**–**D**, **F**–**H**, and **J**–**L**).

results support the notion that the OHC degeneration seen in the *Tric*$^{R497X/R497X}$ mice is mainly due to extracellular factors and not due to the signaling events within an OHC.

To ensure that the rescue phenotype seen in the double-mutant mice was not a consequence of delayed OHC development, we also analyzed the cochlear sensory epithelia of 1- to 2-month-old *Tric*$^{R497X/R497X}$*: Pou3f4*^{delJ} mice. The cochlear sensory epithelia were largely preserved in these older double mutants, as shown by prestin and rhodamine phalloidin labeling (Supplemental Figure 12, A–C). Furthermore, prestin labeling (38) was unaltered in the *Tric*$^{R497X/R497X}$*: Pou3f4*^{delJ} mice at P7 compared with that observed in control *Tric*$^{R497X/+}$*: Pou3f4*$^{+}$ littermates (Supplemental Figure 12, D and E). Taken together, these results favor the hypothesis that the OHC development is not delayed in the *Tric*$^{R497X/R497X}$*: Pou3f4*^{delJ} double mutants and the rescue of OHC degeneration is attributed to dramatic changes of endolymph associated with the loss of POU3F4.

Tric$^{R497X/R497X}$ *mice have syndromic deafness*. Despite the ubiquitous expression of tricellulin, mutations in this gene lead to hearing loss (DFNB49), with no apparent other clinical phenotype in humans (24). However, no comprehensive clinical evaluations of the affected individuals of the DFNB49 families have been reported so far. Therefore, to assess potential deficits of *Tric* knockin mutant mice in other tissues, we performed histopathological examination of 41 tissues, hematological evaluation, and a panel of chemistry tests of serum derived from *Tric*$^{R497X/R497X}$, *Tric*$^{R497X/+}$, and *Tric*$^{+/+}$ littermates at 3 months of age (see Figure 8, Supplemental Figure 13, and Supplemental Tables 2 and 3). Overall, the body weights of *Tric*$^{R497X/+}$ and *Tric*$^{R497X/R497X}$ mice were higher, while the weights of brains were similar among all 3 genotypes (Supplemental Figure 13, A and B). *Tric*$^{R497X/R497X}$ mice had significantly larger heart, spleen, liver, and kidney ratios individually compared with brain weights (Supplemental Figure 13, C–F). As an indicator of functions of these organs, we evaluated the serum biochemical parameters. Levels of several biochemical parameters were higher in the *Tric*$^{R497X/R497X}$ and *Tric*$^{R497X/+}$ animals compared with those in the *Tric*$^{+/+}$ mice (Supplemental Table 2). However, as the values were still largely within the normal reference range, it is unlikely that the results reflect a bona fide instance of an abnormality. As compared with those of wild-type and *Tric*$^{R497X/+}$ mice, we observed changes in the mandibular salivary glands and thyroid follicles of the *Tric*$^{R497X/R497X}$ mice (Figure 8). All of the 6 *Tric*$^{R497X/R497X}$ mice had altered histology of the granular ducts of the mandibular salivary glands (Figure 8, A–F). While all the males had a decrease in granules (Figure 8, A–C), the females had depletion of the granules (Figure 8, D–F). The production of these granules is thought to be coordinated with the levels of testosterone. The *Tric*$^{R497X/R497X}$ mice also had a significantly elevated number of

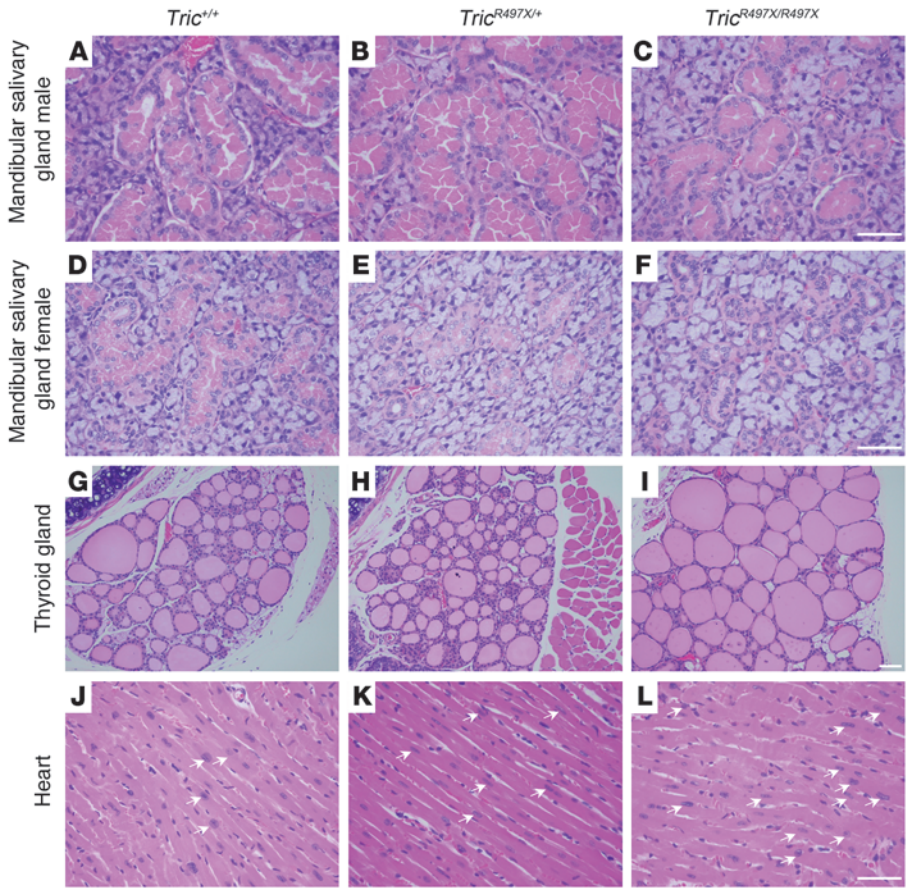

Figure 8
p.Arg497* mutation results in phenotypic changes in the cellular structures of various organs. Hematoxylin and eosin staining of paraffin-embedded sections of the various organs of (**A**, **D**, **G**, and **J**) *Tric*$^{+/+}$ (n = 5), (**B**, **E**, **H**, and **K**) *Tric*$^{R497X/+}$ (n = 6), and (**C**, **F**, **I**, and **L**) *Tric*$^{R497X/R497X}$ (n = 6) mice. Images are of (**A**–**C**) mandibular salivary glands of male mice, (**D**–**F**) mandibular salivary glands of female mice, (**G**–**I**) thyroid glands, and (**J**–**L**) hearts. In general, the *Tric*$^{R497X/R497X}$ males appeared to have a decrease in the number of granules in the mandibular salivary gland, while females had a depletion of granules. The thyroid glands of *Tric*$^{R497X/R497X}$ mice had a significantly elevated number of ectatic follicles (P < 0.05), and there was a higher number of myocytes with enlarged nuclei (arrows) in the *Tric*$^{R497X+}$ and *Tric*$^{R497X/R497X}$ mice. Scale bar: 50 μm.

ectatic thyroid follicles (Figure 8, G–I; P < 0.05). This suggests that these follicles contain more thyroglobulin either due to overproduction of the thyroid hormone precursor or due to lesser uptake. Although detailed cellular and functional evaluation is required, it is tempting to speculate that tricellulin deficiency may lead to a partial loss of the tight junction fence function and a subsequent change in the number of thyroglobulin receptors available at the apical surface of thyrocytes.

Both *Tric*$^{R497X/+}$ and *Tric*$^{R497X/R497X}$ mice had morphological changes associated with the tricellulin mutation in the rostral olfactory epithelium and the heart (Figure 8 and data not shown). A previous study has shown that tricellulin is expressed at tricellular tight junctions in the human olfactory epithelium, and the authors propose that the protein may be necessary to seal the tricellular contacts against inhaled viruses and antigens (23). Finally, enlarged nuclei were seen in a large number of myocytes from the *Tric*$^{R497X/+}$ and *Tric*$^{R497X/R497X}$ mice (Figure 8, J–L). This suggests that the mutation may lead to myocardial hypertrophy of the heart, at least in the murine model of DFNB49.

Discussion

This is the first study describing the pathophysiology of DFNB49, a recessive nonsyndromic deafness. DFNB49 is associated with mutations in tricellulin, a tight junction protein found at all tricellular tight junctions in the cochlear duct (24). Based on the known nonsense mutation, p.Arg500*, which underlies DFNB49, we developed a corresponding mouse model (p.Arg497*). Tricellulin was absent from the tricellular tight junctions in all sensory and nonsensory epithelia of the inner ear organs of *Tric*$^{R497X/R497X}$ mice, which allowed us to study, for the first time, the effects of tricellulin deficiency in vivo. Our RT-PCR assays revealed novel *Tric* transcripts (*Tric-d* and *Tric-e*). These alternate transcripts could potentially have different intracellular interactors compared with full-length isoforms, due to lack of one or more cassette exons encoding part of the cytoplasmic region of tricellulin. The real-time assays revealed differential regulation of various *Tric* isoforms in *Tric*$^{R497X/R497X}$ mutant mice (Supplemental Figure 1A). However, as expected, the full-length tricellulin protein was not detectable by Western blot analysis in inner ears of *Tric*$^{R497X/R497X}$ mutant mice, and there was no tricellulin immunoreactivity at the level of tight junctions (Figure 1F and Supplemental Figure 1B). Moreover, the mutant mice had ultrastructural changes in the tricellular junctions and displayed cochlear hair cell loss, suggesting that the differentially regulated shorter tricellulin isoforms cannot compensate for the loss of the full-length protein.

We found that loss of tricellulin prevented the coalition of the strands of the bicellular junction with the central element of the tricellular junction in the inner ear epithelia of *Tric*$^{R497X/R497X}$ mice (Figure 5 and Supplemental Figures 7 and 8). These ultrastructural changes are in agreement with previous results suggesting that tricellulin may be required for functional continuity of tight junctions at tricellular contacts and that, in tricellulin knockdown cells, small gaps in occludin labeling are often seen at tricellular junctions (8). This disruption in tricellular junctions may create a

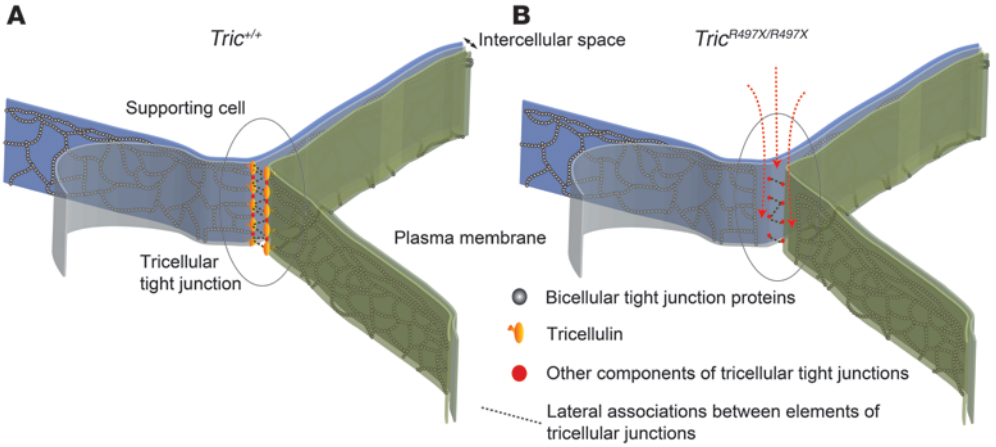

Figure 9

Absence of tricellulin may lead to paracellular permeability barrier defects. Illustrations of the en face views of the proposed ultrastructural appearance of tricellular tight junctions in the reticular lamina of (**B**) *Tric*$^{R497X/R497X}$ mice compared with that in (**A**) *Tric*$^{+/+}$ mice, where the third cell is not depicted to provide the "en face" view of the junction components. The intramembranous particles formed by bicellular tight junction proteins are shown between the plasma membrane lipid bilayers. These proteins form lateral associations with junctional proteins in the adjacent cell obliterating the intercellular space. (**A**) At tricellular junctions in *Tric*$^{+/+}$ mice, tricellulin and other proteins from the 3 cells associate with each other to form the central sealing elements, where the bicellular junction strands unite with it. (**B**) In the absence of tricellulin, the tricellular junctions are no longer continuous and the disconnected particles are possibly formed by other as yet unknown proteins. These strands are no longer able to associate with the elements of the bicellular junctions, potentially resulting in "channels" or conduits for paracellular permeability and barrier defect in the *Tric*$^{R497X/R497X}$ mice. The arrows depict paracellular leak of ions or small signaling molecules through the "channels" at the tricellular junctions of *Tric*$^{R497X/R497X}$ mice.

"channel" or conduit for paracellular transport of ions and macromolecules (Figure 9). Knockdown studies in EpH4 and Caco-2 cells suggest that tricellulin is necessary to regulate the paracellular ion permeability in these cell lines (8, 20, 27). Thus, the ultrastructural changes in the tricellular junctions of the *Tric*$^{R497X/R497X}$ mice may indeed lead to changes in the barrier properties of the various epithelia lining the inner ear sensory compartments. Alternatively, defects in tricellulin may lead to intrinsic signaling defects that cause impaired hair cell function, leading to hearing loss.

The exact constituents of the tricellular junction are not yet known, and tricellulin may either be necessary only to form links between bicellular and tricellular junctions or may also be needed to complete the central elements of the tricellular junction. The presence of discontinuous particles in the tricellular tight junction region in the inner ear epithelia of *Tric*$^{R497X/R497X}$ mice (Figure 5, D, F, and G, and Supplemental Figure 8C) suggests that other proteins are also involved in the formation of these cellular junctions. So far, only tricellulin and lipolysis-stimulated lipoprotein receptor have been reported to be tricellular tight junction–associated proteins (8–10, 24, 26). Recently, immunoglobulin-like domain containing receptor 1 (ILDR1) and ILDR2, two LSR-related proteins, have been shown to localize to tricellular contact sites and are potentially involved in the recruitment of tricellulin to tricellular contact sites (39). However, only ILDR1 was expressed in the organ of Corti, including hair cells, while LSR immunoreactivity was restricted to the Claudius cells in this sensory epithelium and ILDR2 was undetectable in the inner ear (39). Therefore, it is plausible that the tricellular tight junctions between cochlear hair cells and supporting cells might be composed of two or more proteins, and, in the absence of tricellulin, the other proteins are able to form discontinuous tricellular tight junctions in the inner ear (Figures 5 and 9 and Supplemental Figure 8). In support of this hypothesis, we found that ILDR1 was localized at the tricellular tight junctions in the organ of Corti of *Tric*$^{R497X/R497X}$ mice at P2 (Supplemental Figure 9).

Apparently, abnormalities of tricellular junctions in *Tric*$^{R497X/R497X}$ mice do not affect the organ of Corti development until approximately P16, when signs of OHC degeneration were evident (Figure 3). This suggests that tricellulin is not necessary for the development of cochlear hair cells but is important for their survival. Degeneration of hair cells in *Tric*$^{R497X/R497X}$ mice may be initiated by either intracellular or extracellular factors. Because the disruption of the stria vascularis and endolymphatic environment with *Pou3f4* deletion rescues the cochlear hair cell phenotype in the *Tric*$^{R497X/R497X}$ mice (Figure 7), it is likely that extracellular mechanisms play a major role in initiating hair cell degeneration.

Which mechanisms may be responsible for cochlear hair cell degeneration in *Tric*$^{R497X/R497X}$ mice? One possibility is that permeability defects at the level of the reticular lamina may lead to leakage of endolymphatic K^+ into the extracellular space around the OHCs, which is normally filled with perilymph. Increase in K^+ concentration around basolateral surfaces of OHCs may result in prolonged depolarization and shortening of these cells and eventually cell death (40, 41). However, the leakage of endolymphatic K^+ should also decrease the EP, which we didn't observe in *Tric*$^{R497X/R497X}$ mice (Figure 6).

Alternatively, Na^+ leakage from the perilymph into the endolymph, which is normally low in Na^+, may increase the concentration of this ion around the hair bundle. As the mechanotransduction channels are nonselective cation channels, a higher concentration of Na^+ around the hair bundle can lead to Na^+ influx into hair cells. Because the OHCs possess very limited abilities to actively remove Na^+ from the cytosol, Na^+ overloading may lead to cellular dysfunction and degeneration (42–44). However, the tricellulin mutant mice have normal EP, and, therefore, the high positive potential is expected to inhibit the movement of Na^+ ions from the perilymph into the endolymph substantially.

In correspondence with previous reports (9), tricellulin is essential for regulation of paracellular transport of small uncharged molecules but not charged ions. Therefore, disrupted tricellular junctions may increase paracellular flux of important signaling molecules, e.g., extracellular ATP. Purinergic signaling in the cochlea is known to be involved in modulating the auditory neurotransmission in both developing and adult cochleae, maintaining

cochlear homeostasis and the neural reorganization during postnatal development of the cochlea (45). In addition, extracellular ATP-dependent rapid propagation of Ca^{2+} waves is suggested to signal cochlear tissue injury response and can be elicited by the death of a single hair cell (46, 47). ATP receptors are present on the endolymphatic surface of the sensory epithelium as well as the postsynaptic specializations of synapses between hair cells and neurites of spiral ganglion neurons (45). Thus, improper levels of ATP around the apical and basolateral regions of hair cells may interfere with normal purinergic signaling pathways in these cells as well as synaptic transmission and accurate encoding of sound. In the *Tric*$^{R497X/R497X}$*: Pou3f4*^{delJ} mice, the altered microenvironment of the endolymph, due to loss of POU3F4, may result in removal of the extracellular factors that lead to cellular insult in the organ of Corti due to the tricellulin knockin mutation. Certainly, ATP is not the only signaling molecule that could permeate the abnormal tricellular junctions in *Tric*$^{R497X/R497X}$ mice.

Although all the sensory organs of the inner ear express tricellulin at the tricellular tight junctions, the protein appears to be absolutely necessary only in the cochlea. Such a specific defect may either reflect different functional roles played by the protein in the various epithelia involved or may be the result of functional compensation by other tight junction proteins in all inner ear epithelia except the organ of Corti. A previous study produced a spatial expression profile of several members of the claudin family of tight junction proteins within the inner ear. Although most of these claudins are expressed in multiple cell types, claudin 11 expression is restricted to the tight junctions of the basal cell layer of the stria vascularis (48). It is interesting that the expression patterns of claudins 2, 8, and 10 conform to those of tight junction candidates that may be functionally compensating for the loss of tricellulin at the stria vascularis and Reissner's membrane but not in the organ of Corti. These claudins are expressed at the former two epithelia but are not present at the tight junctions of the reticular lamina (48). It is now known that the combination of the various claudins expressed in a particular epithelium dictate the permeability properties of that epithelium (49, 50). Thus, based on the function of the epithelia, the cells express the claudins that confer the necessary permeability barriers. In this regard, it is important to point out that the reticular lamina differs from the other types of epithelia in the cochlear duct. The reticular lamina experiences considerable mechanical stress from the electromotile property of the OHCs as well as the movements of the endolymph and the tectorial membrane and the basilar membrane that push the hair bundles in one direction or another (51–53). Moreover, the tricellular tight junctions in the organ of Corti are unique in comparison to those in other epithelia, in that they extend the entire depth of the reticular lamina, a region spanning approximately 5 μm. In view of the idea that the tight junctions are dynamic structures, being modified in response to external and internal cues, tricellulin may be uniquely important to maintain the integrity of the reticular lamina in the presence of continually varying mechanical stress. Thus, in the *Tric*$^{R497X/R497X}$ mice, sound-induced vibrations may cause excessive stretching of the tricellular tight junctions in the reticular lamina, making it more susceptible to paracellular barrier defects. Tricellulin deficit in other cell types in the inner ear may not result in an observable phenotype, as these tissues do not experience the types of forces seen at the apical surface of the cochlear sensory epithelium.

In summary, our characterization of the tricellulin mutant mice provides insights into the pathogenesis of deafness due to *TRIC* mutations and further demonstrates the biological significance of tricellulin in regulating the paracellular barrier in the organ of Corti and other body organs. The phenotypic changes observed in the other organs of the DFNB49 mouse model suggest a more widespread requirement of this tricellular tight junction protein. In the previous studies, the affected members of the DFNB49 families did not reveal any other obvious phenotypes besides prelingual, sensorineural hearing loss (24, 28, 29). However, the human families were not assessed to the same extent as the phenotypic evaluation of the tricellulin mutant mice. Thus, the affected members of the DFNB49 families may have other as yet unreported disorders. In light of the current observations, we are beginning to understand the broader function of tricellulin, and this study will guide us further for follow-up clinical evaluations of human families and help us understand the complete phenotypic spectrum.

Methods

Mutant mice and genotyping. The orthologous *Tric* mutation in mice to the human p.Arg500* nonsense allele is p.Arg497*, due to few amino acid changes in evolutionary nonconversed regions of the protein. To generate *Tric*$^{R497X/R497X}$ mice, a 12-kb region, including exons 5 and 6 and the surrounding intronic regions, was amplified from genomic DNA of 129X1/SvJ mice and used to construct the targeting vector. The vector was designed to include exons 5 and 6, which were flanked by loxP sites. A neomycin resistance cassette that was flanked by FRT sites was included upstream of exon 5. The nonsense knockin mutation was introduced by site-directed mutagenesis. The targeting construct was electroporated into the 129X1/SvJ embryonic stem cells. A total of 400 embryonic stem cells were screened for homologous recombination events by Southern blot analysis, with probes located both 5′ and 3′ to the integration site. Eighteen recombinant clones were identified, and 3 of them were used for injection into C57BL/6J blastocysts to generate chimeric mice. Mice heterozygous for the targeted allele were obtained by mating male chimeras with C57BL/6J females. Germline transmission was confirmed by Southern blot and PCR analyses. Mice used in this study were maintained on a mixed background of 129X1/SvJ and C57BL/6J. Genotyping using the forward and reverse primers (Supplemental Table 1) produced a PCR product of 440 bp for the wild-type allele, whereas the p.Arg497* allele produced a 579-bp product (Figure 1C).

RT-PCR and real-time PCR assays. Total RNA was isolated from P10 inner ear tissue dissected from 5 *Tric*$^{R497X/R497X}$ mice and control littermate mice using TRIzol reagent (Invitrogen). cDNA was prepared using an oligo-dT primer and SMARTScribe Reverse Transcriptase (Clontech). To determine the structure and isoforms of *Tric*, primers placed in exon 3 and exon 8 were used for PCR (Supplemental Table 1). All PCR products were subcloned into the Topo TA-cloning vector (Invitrogen), and both strands were fully sequenced.

Real-time TaqMan assays were designed to detect the various *Tric* isoforms (Supplemental Table 1). One TaqMan assay was designed to collectively detect isoforms *Tric-a* to *Tric-d*, while the remaining assays specifically amplify *Tric-d* and *Tric-e*, respectively (Supplemental Table 1). The assays were performed in triplicate using the P10 *Tric*$^{+/+}$ (n = 5) and *Tric*$^{R497X/R497X}$ (n = 5) inner ear cDNA libraries and ABI StepOne Plus analyser (Life Technologies). CT values were normalized using *Gapdh* as an endogenous control, and fold changes of expression of *Tric* isoforms were calculated using SA Biosciences online software (http://pcrdataanalysis.sabiosciences.com/pcr/arrayanalysis.php). The significance of the fold change is shown as a P value based on a Student's t test analysis.

Immunofluorescence. For all tight junction labeling, the inner ears extracted from mice were fixed in cold 2 N trichloroacetic acid (TCA) for 18 minutes or 10% TCA for 20 minutes (ILDR1 labeling), followed by

3 washes with PBS. The cochleae were finely dissected in PBS, in which the stria vascularis was removed and the spiral ligament was cut off to expose the sensory epithelium. The cochlear coils were cut into apical, middle, and basal pieces and permeabilized in 0.2% Triton X-100 for 20 minutes, before incubating in preblock (5% BSA, 2% normal goat serum in PBS) for 1 hour. The tissue samples were probed with primary antibody for 2 hours and, after 3 washes, were probed with the secondary antibody for 20 minutes at room temperature. The tricellulin antibody PB705 (24) was used at 1:200 dilution, and the ZO-1 mouse antibody (Invitrogen) was used at 1:100 dilution. The ILDR1 antibody was a gift from Mikio Furuse (Division of Cell Biology, Department of Physiology and Cell Biology, Kobe University Graduate School of Medicine, Kobe, Japan) (39). Rabbit antibodies to ZO-2 and claudin 3, 5, and 10 were purchased from Invitrogen and used at 1:100.

For hair cell body labeling, an in-house antibody raised against prestin was used at 1:200 dilution, calretinin (Abcam) was used at 1:100, and myoVIIa (Proteus Biosciences) was used at 1:250. Here, the inner ears were fixed with 4% paraformaldehyde overnight at 4°C and permeabilized with 0.2% Triton X-100, followed by incubation in blocking solution containing 2% BSA and 5% normal goat serum for 1 hour. The formaldehyde-fixed cochleae were probed overnight with primary antibody and, after 3 washes, were probed with the secondary antibody for 20 minutes. For all hair cell staining, rhodamine-conjugated phalloidin (Invitrogen) was used at 1:300 dilution to visualize the cuticular plate and hair bundles.

For the tricellulin (PB705), prestin, and myoVIIa antibodies, Alexa Fluor 488 goat anti-rabbit secondary antibody (Invitrogen) was used at 1:500 dilution. For ZO-1 antibody, Alexa Fluor 546 goat anti-mouse secondary antibody (Invitrogen) was used at 1:500, and for calretinin antibody, Alexa Fluor 647 goat anti-rabbit secondary antibody (Invitrogen) was used at 1:400 dilution. When used, DAPI was used at 20 μg/ml. After every secondary antibody incubation, the tissues were washed 3 times in PBS and mounted on slides using Vectashield (Vector Laboratories) or ProLong-Gold (Invitrogen) mounting medium and viewed under a LSM meta 700 or LSM780 confocal microscopes (Zeiss Microimaging Inc.) using a ×63, 1.4 N.A. oil-immersion lens. Where necessary, the images were adjusted for optimal brightness and contrast using Photoshop Creative Suite CS5.1.

Western blots. Inner ears were collected from 2 mice for each genotype (*Tric*$^{+/+}$, *Tric*$^{R497X/+}$, and *Tric*$^{R497/R497X}$ mice) in cold lysis buffer (150 mM NaCl, 0.05 M Tris, 1% Triton X-100, and cocktail of protease inhibitors [Roche]). The tissues were homogenized in 1.5-ml tubes with a plastic pestle and sonicated. The lysates were then centrifuged at 21,000 *g* for 20 minutes at 4°C, and the supernatants were collected in fresh tubes and mixed with reducing sample buffer and boiled for 5 minutes. The samples were centrifuged at 21,000 *g* for 5 minutes before loading on a 10% SDS-PAGE gel (Invitrogen). Western blots were carried out using iBlot (Invitrogen), and the proteins were transferred onto nitrocellulose membranes. The membrane blots were blocked with 5% milk for at least 2 hours before probing with rabbit anti-tricellulin polyclonal antibody (Proteintech, catalog no. 13515-1-AP; 1:250 dilution) overnight at 4°C. Blots were probed with anti-HRP secondary antibody (GE Healthcare) used at 1:1,000 dilution. The Western blots were developed using ECL reagents (GE Healthcare).

Cryosections and hematoxylin and eosin staining. Inner ears were collected and fixed for 4 hours at room temperature in 4% paraformaldehyde. After washing out the fixative with PBS, the cochleae were decalcified in 0.25 M EDTA for 1 to 2 days at 4°C. The inner ears were then infiltrated with 30% sucrose in PBS overnight at 4°C, embedded in OCT, and frozen on ethanol/dry ice mix. The frozen tissue blocks were sectioned on a cryotome at 10-μm thickness and processed for hematoxylin and eosin staining. Slides were imaged using a ×40 oil immersion lens on a Zeiss Axioplan Apotome equipped microscope.

ABR and DPOAE measurements. Hearing function was evaluated by ABR analyses at 3 ages (P16, P22, and P30) on 10 to 12 mice of each genotype (*Tric*$^{R497X/R497X}$, *Tric*$^{R497X/+}$, *Tric*$^{+/+}$ mice). Mice were anesthetized with intraperitoneal injections of 2.5% Avertin (0.015 ml/g body weight, Sigma-Aldrich). All recordings were done in a sound-attenuated chamber using an auditory-evoked potential diagnostic system (Intelligent Hearing Systems) with high frequency transducer, as previously described (54). Responses to 50-μs duration clicks and 8-, 16-, and 32-kHz tone-bursts were recorded. Thresholds were determined in 5- or 10-dB steps of decreasing stimulus intensity until waveforms lost reproducible morphology. The maximum sound intensity tested for each frequency was 110 dB sound pressure levels (SPL).

DPOAEs were recorded from mice at P16 to P17 (n = 8–10) with an acoustic probe (ER-10C, Etymotic Research) using DP2000 DPOAE measurement system version 3.0 (Starkey Laboratory). Two primary tones, with a frequency ratio of f_2/f_1 = 1.2, where f_1 represents the first tone and f_2 represents the second, were presented at intensity levels L_1 = 65 dB SPL and L_2 = 55 dB SPL. f_2 was varied in one-eighth octave steps from 8 to 16 kHz. DP grams comprised $2f_1$–f_2 DPOAE amplitudes as a function of f_2.

Vestibular-evoked potential measurements. Vestibular function was evaluated using vestibular-evoked potential recordings at P30 and P150 for 3 mice of each genotype (*Tric*$^{R497X/R497X}$ and *Tric*$^{R497X/+}$ mice). Mice were anesthetized with a mixture of ketamine (90–126 mg/kg, Sigma-Aldrich) and xylazine (10–14 mg/kg, Sigma-Aldrich) injected intraperitoneally. Recordings were completed as previously described (55). Linear acceleration ramps (17 pulses per s, 2-ms duration) were presented to the cranium in the naso-occipital axis. A noninvasive head clip was used to secure the head to a mechanical shaker for delivery of vestibular stimuli. Stimulus levels were quantified in decibels relative to 1.0 *g*/ms (1.0 *g* = 9.8 m/s^2) and ranged from +6 to –18 dB relative to 1.0 *g*/ms adjusted in 3-dB steps. Peak latencies (in milliseconds), peak-to-peak amplitude (in microvolts), and thresholds (in dB relative to 1.0 *g*/ms) were quantified and compared among genotypes.

Freeze-fracture analysis. For freeze-fracture analysis, the inner ears were removed from animals after decapitation, and the cochleae were exposed. The oval and round windows were opened, and a small piece of bone was removed from the cochlear apex. Fixative (2.5% glutaraldehyde in 0.1 M cacodylate buffer with 3 mM $CaCl_2$) was gently injected into the inner ear through these openings, and the entire bulla was then immersed in fixative. Fixation continued for 1.5 hours at room temperature, with gentle, slow rotation. Inner ear tissue was dissected from the bulla and was incubated for at least 45 minutes in 25% glycerol before mounting on freeze-fracture planchettes and freezing in propane/isopentane (4:1) cooled in liquid nitrogen. Freeze fracture was performed in a Balzers BAF400D apparatus by use of standard procedures (56) and was viewed on a JEOL 1200EXII microscope. Digital images were adjusted in Photoshop 6.0 (Adobe) for optimal contrast and brightness.

Scanning electron microscopy. For the scanning electron microscopy analysis, the inner ears were removed from animals after decapitation, and the cochleae exposed. A small piece of bone was removed from the cochlear apex, and the entire bulla was immersed in fixative (2.5 % glutaraldehyde, 0.1 M sodium cacodylate containing 2 mM $CaCl_2$ for 1.5 hours). After 3 quick washes with 0.1 M sodium cacodylate buffer, the inner ears were post-fixed in 1% osmium tetroxide in 0.1 M sodium cacodylate buffer for 1 hour at room temperature. The inner ears were washed 3 times with PBS buffer before incubating in PBS containing 0.25 M EDTA for 2 days at 4°C. The samples were then finely dissected in water to remove the stria vascularis, and the spiral ligament was cut off to expose the organ of Corti. The cochlear tissues were then dehydrated in acetone, critical point dried, sputter coated with gold, and imaged on a scanning electron microscope. Where necessary, the images were adjusted for optimal brightness and contrast using Photoshop Creative Suite CS5.1.

Tracer assay. Temporal bones were removed from mice (P30, 8 months and 10 months of age), and the round and oval windows were opened

in PBS containing 1 mM $CaCl_2$. The perilymphatic space was carefully perfused with 100 μl of 10 mg/ml^{-1} EZ-Link Sulfo-NHS-LC-Biotin (Pierce Chemical) in PBS containing 1 mM $CaCl_2$ for 5 minutes, followed by perfusion with PBS containing 1 mM $CaCl_2$ 5 times. The temporal bones were then fixed by perilymphatic perfusion with 10% TCA for 1 hour and processed for immunofluorescence microscopy. The distribution of injected biotin tracer was visualized by incubating frozen sections with streptavidin/FITC (Oncogene Research Products) for 30 minutes.

Cell lines and transfections. The tricellulin constructs TRIC^{WT} and TRIC^{R500X} in pEGFP C2 vectors (Invitrogen) were a gift from Alan Fanning (Department of Cell Biology and Physiology, University of North Carolina, Chapel Hill, North Carolina, USA). For transfections, cells were plated at 60% confluency on glass coverslips in 35-mm dishes and transfected the following day with the tricellulin constructs using Fugene HD (Promega) according to manufacturer's protocol. Transfected cells were typically examined after 48 hours, fixed, and processed for immunofluorescence as above.

Cochlear explants. Organ of Corti explants dissected from wild-type and *Tric*$^{R497X/R497X}$ mice at P3 were placed in glass-bottom Petri dishes (MatTek Corporation) and cultured in DMEM medium supplemented with 7% fetal bovine serum (Invitrogen) and 10 mg/ml ampicillin (Calbiochem) at 37°C, 5% CO_2, as previously described (57). Briefly, after opening the cochlea and separating the lateral wall, the sensory epithelium was dissociated from modiolus. The epithelium containing the whole length of the organ of Corti, except the most basal "hook" region, was uncoiled and placed into the Petri dish. The organ of Corti explants were then kept in vitro for 3 to 5 days before the experiments. Experiments were performed in hair cells located at 45% to 70% of the whole length of the cochlea from the apex. The equivalent ages (age of dissection plus days in vitro) of the specimens were P6–P8.

Whole-cell patch-clamp recording. The experiments were performed in L-15 cell culture medium (Invitrogen) containing the following inorganic salts: NaCl (137 mM), KCl (5.4 mM), $CaCl_2$ (1.26 mM), $MgCl_2$ (1.0 mM), Na_2HPO_4 (1.0 mM), KH_2PO_4 (0.44 mM), and $MgSO_4$ (0.81 mM). OHCs were observed with an upright microscope using a ×60 1.0 NA 2.0 WD water-immersion objective and differential interference contrast. To access the basolateral plasma membrane of the OHCs, the supporting cells covering OHCs were removed by gentle suction with a ~5-μm micropipette. Smaller pipettes were then used for whole-cell patch-clamp recordings and prefilled with intracellular solution containing: KCl (12.6 mM), potassium gluconate (131.4 mM), $MgCl_2$ (2 mM), EGTA (0.5 mM), K_2HPO_4 (8 mM), KH_2PO_4 (2 mM), ATP-Mg^{2+} (2 mM), and GTP-Na_2 (0.2 mM). Osmolarity and pH of the intrapipette solution were adjusted with D-glucose and KOH to match corresponding values of the bath (316 mOsm, pH = 7.35). The pipette resistance measured in the bath was 4–6 MΩ. Patch-clamp recordings were performed in the third- or second-row OHCs located approximately in the middle of the cultured organ of Corti explants with a computer-controlled amplifier (Cairn Optopatch, Cairn Research Ltd.). Membrane potentials were corrected for the voltage drop across series resistance. Between the acquisitions, OHCs were maintained at a holding potential of –60 mV. Membrane currents from third-row or second-row OHCs elicited by hyperpolarizing and depolarizing voltage steps were recorded using pCLAMP 9.0 software (Axon Instruments), prefiltered at 30 kHz, postfiltered at 1.5 kHz, sampled at 5 kHz, and averaged 4 times. All experiments were performed at room temperature.

EP measurements. Mice were anesthetized with isoflurane (1%–2% in oxygen) and placed on a small operating table on their backs. Body temperature was maintained with a heat pad controlled by an animal temperature controller and monitored continuously. The cochlea was accessed via a longitudinal, ventral, paramedian approach, as described previously (58). After exposure of the bulla, a small opening was made with the help of forceps and a microdrill, taking care that the tympanic membrane and the stapes remain intact. For EP measurement, a tiny hole was made in the cochlea in the dark area just above the stapedial artery. An electrode filled with a concentrated KCl solution (2 M) was advanced through the hole using a hydraulic 1-dimensional micromanipulator (Narishige), and its potential was continuously monitored with an Cyto 721 Electrometer (WPI). Abrupt changes of the potential to a new steady-state level indicated penetration into the scala media. Measurement of EP was considered successful if the EP was stable for at least 30 seconds and the potential returned to zero when the electrode was retracted out of the cochlea.

Serum chemical, hematological, and histological analysis. Sera derived from 6 mice of each genotype (*Tric*$^{R497X/R497X}$, *Tric*$^{R497X/+}$, and *Tric*$^{+/+}$ mice) with 129X1/SvJ and C57BL/6J mixed background at 3 months of age were analyzed by the Division of Veterinary Resources at NIH (http://www.ors.od.nih.gov/sr/dvr/drs/Pages/Mouse%20Phenotyping.aspx). The analysis included complete serum chemistries and electrolytes, liver function tests, creatine kinase, GGTP, amylase, lipase, cholesterol, triglycerides, and uric acid.

The histopathological analysis included evaluation by hematoxylin and eosin staining of gross and microscopic changes in a panel of tissues (as listed in the Results) obtained from 6 mice of each genotype (*Tric*$^{R497X/R497X}$, *Tric*$^{R497X/+}$, and *Tric*$^{+/+}$ mice) at 3 months of age. Standard hematological tests were also performed and included cell counts of white blood cells, neutrophils, lymphocytes, monocytes, eosinophils, basophils, red blood cells, and platelets and levels of hemoglobin, hematocrit, mean corpuscular volume, mean corpuscular hemoglobin, and mean corpuscular hemoglobin concentration. As indicated in Supplemental Figure 13, body and organ weights of all animals were also measured.

Statistics. Statistical analyses were performed using Student's *t* test of independent variables (2-tailed distribution). All average data on the graphs are shown as mean ± SEM (unless indicated otherwise in the figure legends). In all instances, *P* values of less than 0.05 were considered significant.

Study approval. All study protocols involving mice were approved by the Animal Care and Use Committees at Cincinnati Children's Hospital Research Foundation, National Institute on Deafness and Other Communication Disorders, University of Kentucky, University of Nebraska, and University College London and conducted in accordance with the NIH Guide for Care and Use of Laboratory Animals.

Acknowledgments

We thank Thomas Friedman, Zubair Ahmed, Elodie Richard, and Arnaud Giese for critiques of our ideas and manuscript, Elizabeth Wilson for genotyping and maintaining our mouse colonies, and Manna Li and Kira Rehn for technical assistance. We also thank Penelope Friedman for her review of the *Tric* knockin mice biochemical and histology results. This work was supported by a Deafness Research Foundation grant, Action on Hearing Loss grant, and National Institute on Deafness and Other Communication Disorders (NIDCD/NIH) research grants (R01 DC011748 and DC011803 to S. Riazuddin; R01 DC006443 to S.M. Jones; R01 DC009434 to G.I. Frolenkov; the intramural funds from NIDCD DC000039-15) as well as the International Center for Genetic Engineering and Biotechnology, Trieste, Italy (project CRP/PAK08-01).

Received for publication January 28, 2013 and accepted in revised form May 30, 2013.

Address correspondence to: Saima Riazuddin, Laboratory of Molecular Genetics, Cincinnati Children's Hospital Research Foundation, 3333 Burnet Avenue, MLC2018, Cincinnati, Ohio 45229, USA. Phone: 513.803.2888; Fax: 513.803.2899; E-mail: Saima.Riazuddin@cchmc.org.

1. Tsukita S, Yamazaki Y, Katsuno T. Tight junction-based epithelial microenvironment and cell proliferation. *Oncogene*. 2008;27(55):6930–6938.
2. Van Itallie CM, Anderson JM. Claudins and epithelial paracellular transport. *Annu Rev Physiol*. 2006;68:403–429.
3. Yap AS, Mullin JM, Stevenson BR. Molecular analyses of tight junction physiology: insights and paradoxes. *J Membr Biol*. 1998;163(3):159–167.
4. Schneeberger EE, Lynch RD. The tight junction: a multifunctional complex. *Am J Physiol Cell Physiol*. 2004;286(6):C1213–C1228.
5. Steed E, Balda MS, Matter K. Dynamics and functions of tight junctions. *Trends Cell Biol*. 2010; 20(3):142–149.
6. Balda MS, Matter K. Tight junctions and the regulation of gene expression. *Biochim Biophys Acta*. 2009;1788(4):761–767.
7. Sasaki H, Matsui C, Furuse K, Mimori-Kiyosue Y, Furuse M, Tsukita S. Dynamic behavior of paired claudin strands within apposing plasma membranes. *Proc Natl Acad Sci U S A*. 2003;100(7):3971–3976.
8. Ikenouchi J, Furuse M, Furuse K, Sasaki H, Tsukita S, Tsukita S. Tricellulin constitutes a novel barrier at tricellular contacts of epithelial cells. *J Cell Biol*. 2005;171(6):939–945.
9. Krug S, Amasheh S, Richter J. Tricellulin forms a barrier to macromolecules in tricellular tight junctions without affecting ion permeability. *Mol Biol Cell*. 2009;20(16):3713–3724.
10. Mariano C, Sasaki H, Brites D, Brito MA. A look at tricellulin and its role in tight junction formation and maintenance. *Eur J Cell Biol*. 2011;90(10):787–796.
11. Staehelin LA. Further observations on the fine structure of freeze-cleaved tight junctions. *J Cell Sci*. 1973;13(3):763–786.
12. Gulley RL, Reese TS. Intercellular junctions in the reticular lamina of the organ of Corti. *J Neurocytol*. 1976;5(4):479–507.
13. Jahnke K. [Intercellular junctions in the guinea pig stria vascularis as shown by freeze-etching (author's transl)]. *Anat Embryol (Berl)*. 1975;147(2):189–201.
14. Johnstone BM, Sellick PM. Dynamic changes in cochlear potentials and endolymph concentrations. *J Otolaryngol Soc Aust*. 1972;3(3):317–319.
15. Souter M, Forge A. Intercellular junctional maturation in the stria vascularis: possible association with onset and rise of endocochlear potential. *Hear Res*. 1998;119(1–2):81–95.
16. Fanning AS, Anderson JM. Zonula occludens-1 and -2 are cytosolic scaffolds that regulate the assembly of cellular junctions. *Ann N Y Acad Sci*. 2009; 1165:113–120.
17. Tsukita S, Katsuno T, Yamazaki Y, Umeda K, Tamura A, Tsukita S. Roles of ZO-1 and ZO-2 in establishment of the belt-like adherens and tight junctions with paracellular permselective barrier function. *Ann N Y Acad Sci*. 2009;1165:44–52.
18. Furuse M, Sasaki H, Tsukita S. Manner of interaction of heterogeneous claudin species within and between tight junction strands. *J Cell Biol*. 1999; 147(4):891–903.
19. Tsukita S, Furuse M, Itoh M. Multifunctional strands in tight junctions. *Nat Rev Mol Cell Biol*. 2001; 2(4):285–293.
20. Raleigh D, Marchiando A, Zhang Y. Tight junction-associated MARVEL proteins marveld3, tricellulin, and occludin have distinct but overlapping functions. *Mol Biol Cell*. 2010;21(7):1200–1213.
21. Steed E, Rodrigues NTL, Balda MS, Matter K. Identification of MarvelD3 as a tight junction-associated transmembrane protein of the occludin family. *BMC Cell Biol*. 2009;10:95.
22. Elkouby-Naor L, Ben-Yosef T. Functions of claudin tight junction proteins and their complex interactions in various physiological systems. *Int Rev Cell Mol Biol*. 2010;279:1–32.
23. Ohkuni T, et al. Expression and localization of tricellulin in human nasal epithelial cells in vivo and in vitro. *Med Mol Morphol*. 2009;42(4):204–211.
24. Riazuddin S, et al. Tricellulin is a tight-junction protein necessary for hearing. *Am J Hum Genet*. 2006;79(6):1040–1051.
25. Ikenouchi J, Sasaki H, Tsukita S. Loss of occludin affects tricellular localization of tricellulin. *Mol Biol Cell*. 2008;19(11):4687–4693.
26. Masuda S, et al. LSR defines cell corners for tricellular tight junction formation in epithelial cells. *J Cell Sci*. 2011;124(pt 4):548–555.
27. Van Itallie CM, Fanning AS, Holmes J, Anderson JM. Occludin is required for cytokine-induced regulation of tight junction barriers. *J Cell Sci*. 2010; 123(pt 16):2844–2852.
28. Chishti MS, et al. Splice-site mutations in the TRIC gene underlie autosomal recessive nonsyndromic hearing impairment in Pakistani families. *J Hum Genet*. 2008;53(2):101–105.
29. Safka Brozkova D, et al. DFNB49 is an important cause of non-syndromic deafness in Czech Roma patients but not in the general Czech population. *Clin Genet*. 2012;82(6):579–582.
30. Maquat LE. Nonsense-mediated mRNA decay: splicing, translation and mRNP dynamics. *Nat Rev Mol Cell Biol*. 2004;5(2):89–99.
31. Marcotti W, Kros CJ. Developmental expression of the potassium current IK,n contributes to maturation of mouse outer hair cells. *J Physiol*. 1999; 520(pt 3):653–660.
32. Ben-Yosef T. Claudin 14 knockout mice, a model for autosomal recessive deafness DFNB29, are deaf due to cochlear hair cell degeneration. *Hum Mol Genet*. 2003;12(16):2049–2061.
33. Nakano Y, et al. A claudin-9-based ion permeability barrier is essential for hearing. *PLoS Genet*. 2009;5(8):e1000610.
34. Kitajiri S, et al. Compartmentalization established by claudin-11-based tight junctions in stria vascularis is required for hearing through generation of endocochlear potential. *J Cell Sci*. 2004;117(Pt 21):5087–5096.
35. Gow A, et al. Deafness in Claudin 11-null mice reveals the critical contribution of basal cell tight junctions to stria vascularis function. *J Neurosci*. 2004;24(32):7051–7062.
36. Minowa O, et al. Altered cochlear fibrocytes in a mouse model of DFN3 nonsyndromic deafness. *Science*. 1999;285(5432):1408–1411.
37. Song MH, et al. Pou3f4 deficiency causes defects in otic fibrocytes and stria vascularis by different mechanisms. *Biochem Biophys Res Commun*. 2011; 404(1):528–533.
38. Belyantseva IA, Adler HJ, Curi R, Frolenkov GI, Kachar B. Expression and localization of prestin and the sugar transporter GLUT-5 during development of electromotility in cochlear outer hair cells. *J Neurosci*. 2000;20(24):RC116.
39. Higashi T, et al. Analysis of the 'angulin' proteins LSR, ILDR1, and ILDR2 - tricellulin recruitment, epithelial barrier function and implication in deafness pathogenesis. *J Cell Sci*. 2013;126(pt 4):966–977.
40. Zenner HP. K+-induced motility and depolarization of cochlear hair cells. Direct evidence for a new pathophysiological mechanism in Meniere's disease. *Arch Otorhinolaryngol*. 1986;243(2):108–111.
41. Zenner HP, Reuter G, Zimmermann U, Fermin C, LePage EL. Transitory endolymph leakage induced hearing loss and tinnitus: depolarization, biphasic shortening and loss of electromotility of outer hair cells. *Eur Arch Otorhinolaryngol*. 1994;251(3):143–153.
42. Kim SH, Marcus DC. Regulation of sodium transport in the inner ear. *Hear Res*. 2011;280(1–2):21–29.
43. Oliver D, Plinkert P, Zenner HP, Ruppersberg JP. Sodium current expression during postnatal development of rat outer hair cells. *Pflugers Arch*. 1997;434(6):772–778.
44. Shi X, Gillespie PG, Nuttall AL. Na+ influx triggers bleb formation on inner hair cells. *Am J Physiol Cell Physiol*. 2005;288(6):C1332–C1341.
45. Housley GD, Bringmann A, Reichenbach A. Purinergic signaling in special senses. *Trends Neurosci*. 2009;32(3):128–141.
46. Gale JE, Piazza V, Ciubotaru CD, Mammano F. A mechanism for sensing noise damage in the inner ear. *Curr Biol*. 2004;14(6):526–529.
47. Lahne M, Gale JE. Damage-induced activation of ERK1/2 in cochlear supporting cells is a hair cell death-promoting signal that depends on extracellular ATP and calcium. *J Neurosci*. 2008;28(19):4918–4928.
48. Kitajiri SI, et al. Expression patterns of claudins, tight junction adhesion molecules, in the inner ear. *Hear Res*. 2004;187(1–2):25–34.
49. Ebnet K. Organization of multiprotein complexes at cell-cell junctions. *Histochem Cell Biol*. 2008;130(1):1–20.
50. Furuse M, Tsukita S. Claudins in occluding junctions of humans and flies. *Trends Cell Biol*. 2006; 16(4):181–188.
51. Nowotny M. Nanomechanics of the subtectorial space caused by electromechanics of cochlear outer hair cells. *Proc Natl Acad Sci U S A*. 2006; 103(7):2120–2125.
52. Ospeck M. Limiting frequency of the cochlear amplifier based on electromotility of outer hair cells. *Biophys J*. 2003;84(2 pt 1):739–749.
53. Tomo I, Boutet de Monvel J, Fridberger A. Sound-evoked radial strain in the hearing organ. *Biophys J*. 2007;93(9):3279–3284.
54. Kitajiri S, et al. Actin-bundling protein TRIOBP forms resilient rootlets of hair cell stereocilia essential for hearing. *Cell*. 2010;141(5):786–798.
55. Jones TA, Jones SM, Vijayakumar S, Brugeaud A, Bothwell M, Chabbert C. The adequate stimulus for mammalian linear vestibular evoked potentials (VsEPs). *Hear Res*. 2011;280(1–2):133–140.
56. Forge A, Davies S, Zajic G. Assessment of ultrastructure in isolated cochlear hair cells using a procedure for rapid freezing before freeze-fracture and deep-etching. *J Neurocytol*. 1991;484(6):471–484.
57. Stepanyan R, Frolenkov GI. Fast adaptation and Ca2+ sensitivity of the mechanotransducer require myosin-XVa in inner but not outer cochlear hair cells. *J Neurosci*. 2009;29(13):4023–4034.
58. Jero J, Tseng CJ, Mhatre AN, Lalwani AK. A surgical approach appropriate for targeted cochlear gene therapy in the mouse. *Hear Res*. 2001;151(1–2):106–114.
59. Rodriguez CI, et al. High-efficiency deleter mice show that FLPe is an alternative to Cre-loxP. *Nat Genet*. 2000;25(2):139–140.